Author/s:
Huang, Y;Chubb, T;Baumgardner, D;deHoog, M;Siems, ST;Manton, MJ

Title:
Evidence for secondary ice production in Southern Ocean open cellular convection

Date:
2017-04-01

Citation:
Huang, Y., Chubb, T., Baumgardner, D., deHoog, M., Siems, S. T. & Manton, M. J. (2017). Evidence for secondary ice production in Southern Ocean open cellular convection. Quarterly Journal of the Royal Meteorological Society, 143 (704), pp.1685-1703. https://doi.org/10.1002/qj.3041.

Persistent Link:
https://hdl.handle.net/11343/292730

# Evidence for secondary ice production in Southern Ocean open cellular convection

Yi Huang[a,b], Thomas Chubb[c], Darrel Baumgardner[d], Mark DeHoog[e],
Steven T. Siems[a,b], and Michael. J. Manton[a]

[a]School of Earth, Atmosphere and Environment, Monash University, Melbourne, Australia

[b]Australian Research Council (ARC) Centre of Excellence for Climate System Science, Monash University, Melbourne, Australia

[c]Snowy Hydro Ltd., Sydney, New South Wales, Australia

[d]Droplet Measurement Technologies, Boulder, USA

[e]Hydro Tasmania, Hobart, Tasmania, Australia

Manuscript for submission to

*Quarterly Journal of the Royal Meteorological Society*

Corresponding Author
Yi Huang
Email: vivian.huang@monash.edu

## Abstract

Ice particles present at temperatures warmer than -9°C were encountered in unexpectedly high number concentrations (up to 54 $L^{-1}$) by an instrumented aircraft over the Southern Ocean (SO), off the southwest coast of Tasmania, Australia, on 07 September 2013. The sampled clouds were precipitating, characterized by mixed-phase, open-cellular shallow convection. These clouds were present within a large-scale environment characterized by cold air advection, in a pristine air mass for over 72 hours. Using a Cloud and Aerosol Spectrometer, aerosol particles (diameters > 0.6 μm) size and number concentrations were measured and ice nucleating particle (INP) number concentrations were estimated with a recognized ice nuclei parameterization scheme. The estimated INP number concentrations were in the range of $10^{-5}$-$10^{-1}$ $L^{-1}$ at temperature above -9°C, which is up to three orders of magnitude less than the ice number concentrations typically observed. The high ice number concentrations are largely consistent with the theoretical values when ice crystals are produced via a splinter production. The evidence suggests that secondary ice processes (likely the Hallett-Mossop mechanism) were playing a key role in generating the high ice number concentrations observed. Satellite observations from an A-Train overpass in the neighborhood during the flight period reveal a qualitatively consistent story, with patchy, mixed-phase (but predominantly supercooled liquid water) clouds observed at cloud-top temperatures around -6°C. Using back trajectory calculations, these clouds are tracked over 23 and 46 hours with A-Train observations. The presence of these clouds is found to be common over the SO during this period of time. This suggests that the ice particles present in a relatively warm temperature range could potentially be commonplace, within the widespread (up to thousands of kilometers) shallow convective cloud fields over the SO. These clouds may have important implication for the energy budget and precipitation production over this climatically important region.

**Key words:** Southern Ocean; mixed-phase clouds; secondary ice processes; aircraft measurements; A-Train satellites

## 1. Introduction

Mixed-phase clouds, in which supercooled liquid water (SLW) and ice crystals coexist within the same volume of air, are commonly observed in the lower troposphere, particularly over mid- and high-latitude oceans (e.g. Shupe et al., 2001; Korolev et al., 2003; Field et al., 2004; McFarquhar et al., 2007; Huang et al., 2012a). The formation and development of ice particles in mixed-phase clouds have a critical influence on cloud radiative properties, lifetime, and precipitation efficiency (Dong and Mace, 2003; Zuidema et al., 2005). However, progress in understanding the formation and evolution of mixed-phase clouds is hindered by difficulties in observing and characterizing the many complex interactions that lead to the glaciation, and dynamics of these clouds.

Primary ice nucleation may begin to form ice in clouds at temperatures as warm as -4°C in the presence of suitable ice nucleating particles (INPs, e.g. Cantrell and Heymsfield, 2005; Hobbs and Rangno, 1985, 1990). Early observations reported, in some instances, fair agreement between the observed ice number concentration and the number of INP (e.g. Cooper, 1986; Mossop, 1985a); however, numerous studies have reported orders of magnitude higher ice number concentrations (e.g. Blyth and Latham, 1993; Harris-Hobbs and Cooper, 1987; Hobbs and Rangno, 1985, 1990), which suggests the potential importance of a secondary ice production mechanism.

Among the several secondary processes that have been proposed, splinter ejection during riming of ice crystals, known as the Hallett-Mossop (H-M) mechanism (Hallett and Mossop, 1974; Mossop and Hallett, 1974; Mossop, 1976), is probably most commonly invoked. The initial in-situ observations that underpin the H-M hypothesis were made in small maritime cumulus clouds off the coast of Tasmania, within an environment of south-westerly airstream with a long over-sea trajectory (Mossop et al., 1970). Initial and subsequent experiments have shown that ice particles are produced during riming within the temperature range from -3 to -8°C, when small droplets (diameter *D* d 13 ¼m) and large drops (*D* e 24 ¼m, particularly SLW) coexist with graupel particles (Saunders and Hosseini, 2001). The proposal of the H-M mechanism has inspired numerous follow-on studies. Observations from various locations across the globe have cited the H-M process to explain the observed ice number concentrations (e.g. Hogan et al., 2005; Ovtchinnikov et al., 2000; Heymsfield et al., 2014; Taylor et al., 2015). Other ice multiplication processes, such as fragmentation of delicate crystals by mechanical influences (Pruppacher and Klett, 1997), ice-ice collisions (Takahashi et al., 1995), breakup and shedding of crystals during sublimation (Bacon et al., 1998; Oraltay and Hallett, 2005), ice nucleation on drop residuals (Beard, 1992) and circulation induced INP entrainment (Prenni et al., 2007), have also been proposed. A comprehensive overview of the current state of the science on secondary ice production is provided by Field at al. (2016), Chapter 7 of the upcoming American Meteorological Society Monograph.

The Southern Ocean (SO), remote from local anthropogenic influences, is renowned for the strongest, annually-averaged wind speed (Vinoth and Young, 2011), the most frequent precipitation (Ellis et al., 2009) and, in particular, the largest fraction of liquid and mixed-phase clouds among the global oceans (Hu et al., 2010). Frontal glaciated clouds are only observed to account for ~ 12 % of the total cloud cover over this region (Mace, 2008). These clouds have been receiving increasing attention in recent years, largely due to their poor representation in climate models and reanalysis products, and consequently, the outstanding uncertainties and biases in the simulated radiative budget (Trenberth and Fasullo, 2010).

Spaceborne and limited in-situ observations have reported that the SO is dominated by clouds in the temperature range of 0 to -20°C (e.g. Huang et al., 2012b), where SLW is prevalent (e.g. Morrison et al., 2010; Huang et al., 2012a; Chubb et al., 2013; Grosvenor et al., 2012). Recent research has hypothesized that the poor representation of SLW in climate models contributes substantially to the biases in the simulated clouds (Bodas-Salcedo et al., 2016). However, it remains an open question as to what extent SLW dominates the cloud thermodynamic phase over the SO. In addition, the spatial-temporal variability in sources, chemical composition, and INP over this region further contribute to significant observational and modelling uncertainties (Burrows et al., 2013).

Precipitation processes over the SO are even more poorly understood. Limited information on cloud microphysics has been gathered from the few historical field campaigns, such as the Aerosol Characterization Experiment (ACE-1, Bates et al., 1995) and the Southern Ocean Cloud EXperiments (SOCEX I and II; Boers et al., 1998), which had other science objectives. By comparing station records at Macquarie Island (54.50°S 158.94°E), reanalysis data sets and CloudSat retrieval products, Wang et al. (2015) reveals that mixed-phase precipitation is commonly present over the SO, and that light precipitation accounts for ~ 82% of the total precipitation fraction. These findings imply that microphysical processes in mixed-phase clouds likely play a critical role in precipitation production in this region, particularly during winter.

Open mesoscale cellular convection (MCC, Wood and Hartmann, 2006; Wood, 2012), which is typically observed in the cold sectors of mid-latitude cyclones (e.g. Field and Wood, 2007) or in cold-air outbreaks over oceans (Atkinson and Zhang, 1996), prevail along the SO storm track (40-60°S). This cloud morphology, which is most pronounced during winter (occurring ~ 50% of the absolute time), is a significant contrast to that over the high-latitude SO where a closed MCC cloud regime is dominant nearly all year round (Muhlbauer et al., 2014). Both observations and modelling studies suggest that open MCC cloud fields differ significantly from closed MCC cloud fields, with the former being associated with heavier drizzle (e.g. Stevens et al., 2005; Ackerman et al., 1993; Wang and Feingold, 2009) and less shortwave reflectance and transmissivity (Muhlbauer et al., 2014). Even light precipitation typical of marine stratocumulus can profoundly impact the radiative properties of marine low clouds (e.g. Wood et al., 2012) via a modification of cloud microphysical characteristics such as cloud effective radius and droplet number concentration. Thus, a better appreciation of physical processes that are shaping the cloud morphologies is a necessary step towards an improved representation of cloud forcing in climate models.

The major objective of this study is to explore the potential role of secondary ice production in open cellular convection over the SO through a focused case study using both in-situ and satellite observations. We will evaluate the airborne measurements that suggest that the observed ice number concentrations exceed what would be expected given the ice nuclei concentrations in this region. We test if these excessive concentrations could be the result of secondary ice production. Computations of back-trajectories are also performed to help identify the air mass history, as well as establishing the wider synoptic context within which secondary ice processes may occur. It is worth noting that the difficulties of determining secondary ice production from in situ measurements and the need for more diverse measurements have been highlighted in Field et al. (2016). As such, this study can be a component of more comprehensive attempts to explore the prevalence of secondary ice production over the SO, and to characterize and understand the nature of clouds and precipitation over this region.

## 2. Data and Methodology

### 2.1. Aircraft Observations

An ongoing collaborative effort between Monash University and Hydro Tasmania in Australia has been the exploration of the SO cloud and precipitation characteristics during Austral winter (May-October). An instrumented Cessna Conquest aircraft, operated by Hydro Tasmania, was the measurement platform for this project (e.g. Huang et al., 2015). A central objective of this project is the evaluation of cloud and precipitation retrieval products from A-Train (Stevens et al., 2002) satellite observations over the SO. As such, many of the flight tracks were aligned with the A-Train satellite overpasses.

Instruments aboard the aircraft include a Droplet Measurement Technologies (DMT) Cloud Aerosol and Precipitation Spectrometer (CAPS, Baumgardner et al., 2001) that incorporates a hot-wire liquid water sensor, a single particle light scattering Cloud and Aerosol Spectrometer (CAS) that measures particles within the nominal size range of 0.6-50 µm in 30 size bins, and a Cloud Imaging Probe (CIP-25), an optical array probe that is used to record 2-D images of larger particles (50 µm-1.55 mm) in 62 size bins with a 25 µm resolution. Bulk cloud water content is also measured using a Science Engineering Associates (SEA, Tolland, CT, USA) WCM-2000 Multi-Element Water Content System (Lilie et al., 2005). This sensor has two independent cylindrical hot-wire elements (0.5 and 2 mm in diameter, conventionally named WCM-021 and WCM-083, respectively) for in-situ liquid water content, and a scooped 4-mm element for total water content (ice plus liquid). Ambient and dew point temperatures are measured using a Meteolabor TP-3S (Meteolabor AG, Switzerland) that is mounted inside a reverse flow housing to avoid wetting of the sensing element by cloud hydrometeors. The data presented were made at a temporal resolution of one second, which corresponds to a spatial scale of approximately 100 m at a typical aircraft true air speed. All aircraft instruments have been calibrated according to the manufacture instructions and the data are quality controlled. Details of data processing techniques and uncertainty estimates of the CAPS and WCM-2000 measurements can be found in Appendix A1-A4.

In addition, we further introduce the calculated variable $r_{32}$, which is defined as the ratio of the third to the second moment of the hydrometeor size distribution derived from the CAS ($r_{32(CAS)}$) and the CIP ($r_{32(CIP)}$) measurements, respectively. For spherical cloud drops, this is simply the effective radius; when used in clouds containing non-spherical ice particles it is a useful indicator of the particle size that is optically important. Similarly, number concentrations measured by the CAS and the CIP were presented separately. To be consistent with the convention in the cloud physics community, number concentrations measured by the

CAS (i.e. scattering probes) were presented in cm$^{-3}$ while number concentrations measured by the CIP (i.e. imaging probes) were presented in L$^{-1}$.

While this in-situ data set proved valuable for studying clouds and precipitation over the measurement-sparse SO, there are some notable limitations due to the lack of several key measured parameters within the project framework. First, measurements of vertical wind velocities were not made and the reliability of the derived horizontal winds is questionable due to the coarse resolution of reported aircraft headings, particularly during turning. Secondly, measurements of aerosol particle properties were not made, other than size and concentration of particles larger than 0.6 μm. In addition, recent studies (e.g. Korolev and Isaac, 2005; Korolev et al., 2011; Lawson, 2011) suggest that shattering of large ice crystals on probe tips and inlets may result in the presence of artificially generated small ice particles on measurements by instruments such as the CAS and CIP. The tips on the arms of the CIP that are designed to mitigate shattering (Korolev et al., 2010) were not installed prior to 2014; further, the interarrival times that may help with phase identification for small particles were not recorded for the CAS. Although some of the particles measured by the CAS may be shattered ice crystals, it is the general consensus in the published literature (e.g. Field et al., 2007) that this becomes an important issue only when ice crystals that are larger than 100 μm are present in significant concentrations. In the present study, those regions of clouds with significant concentrations of ice crystal with diameters greater than 100 μm are identified and the CAS measurements are treated with caution.

Some of the aforementioned caveats are partially overcome by complementing the cloud water content derived from the CAPS with those from the SEA WCM-2000 sensors. For the purpose of cloud phase partitioning, an “ice fraction ($\mu$)” can be derived using measurements from the SEA WCM-2000, following the method developed by Korolev et al. (2003, hereafter K03) which was derived from the Nevzorov probe, a sensor similar to the WCM-2000. In K03, $\mu$ is defined as

$$\mu = \frac{W_{ice}}{W_{ice} + W_{liq}} \quad (1)$$

where $W_{ice}$ and $W_{liq}$ are the ice and liquid water contents derived from the measurements by the Nevzorov probes. The same principle is applied in our study to the SEA WCM-2000 measurements. Details of the calculations are provided in Appendix A3. Following K03 we define "clouds" using the threshold value of total water content $W_{TWC} > 0.01$ g m$^{-3}$. For the purposes of our study, clouds with $\mu < 0.1$ are defined as 'liquid', clouds with 0.1 d $\mu$ d 0.9 as 'mixed phase' and clouds with $\mu > 0.9$ as 'ice'. It should be noted that while we adopt the same methodology as K03 for the calculations of $W_{ice}$ and $W_{liq}$, the coefficients for the Nevzorov and the SEA WCM-2000 sensors are not necessarily identical given that the shapes of the sensors are somewhat different. More dedicated studies are needed to better understand any discrepancies between the measurements from the WCM-2000 and CAPS. This is particularly necessary for the WCM-2000 probe, which is a relatively new sensor and has not received the same level of critical evaluation as other cloud instruments like the CAPS and Nevzorov probes. Nevertheless, in the present study, we only use $\mu$ as a qualitative indicator to constrain the cloud phase partition. Quantitative analysis is not the emphasis in this study but will be explored in future work.

### 2.2. A-Train Satellite Observations

We use cloud and aerosol retrieval products from three A-Train (Stephens et al., 2002; L'Ecuyer and Jiang, 2010) satellites – the Moderate Resolution Imaging Spectroradiometer (MODIS, Platnick et al., 2003) aboard Aqua, CloudSat (Tanelli et al., 2008), and the Cloud-Aerosol Lidar And Infrared Pathfinder Satellite Observations (CALIPSO, Winker et al., 2009). MODIS level-2 cloud products offer a range of retrieved cloud properties such as cloud-top temperature, cloud thermodynamic phase, cloud effective radius, cloud optical thickness, etc., with a spatial resolution of 1×1 km$^2$ or 5×5 km$^2$ at nadir, depending on the channels from which the cloud properties are retrieved. The two active remote sensors - the Cloud-Aerosol Lidar with Orthogonal Polarization (CALIOP) on CALIPSO and the Cloud Profiling Radar (CPR) on CloudSat provide vertical distributions of clouds, aerosol, and precipitation properties along the sub-satellite tracks. We use the CALIPSO Vertical Feature Mask product (VFM, version 3.01) which contains a classification of cloud and aerosol feature within a vertical profile, retrieved primarily from lidar attenuated backscatter and depolarization ratio (Hu et al., 2009; Omar et al., 2009). We use the CPR radar reflectivity from the CloudSat Geometrical Profile product ("2B-GEOPROF", Marchand et al., 2008), thermodynamic variables from the "ECMWF-AUX" product (Partain, 2007), and surface rain rate produced by the 2C-COLUMN-PRECIP product (R04, Haynes et al., 2009). The later contains complementary information produced by the European Centre for Medium-Range Weather Forecasts (ECMWF). A known issue with CloudSat is that radar bins within 750 m of the ocean surface suffer from surface clutter contamination (Marchand et al., 2008). Accordingly, the CPR may provide only limited insights for cloud properties within the boundary layer. As will be demonstrated later this issue does not affect the analysis of this study. Nevertheless, CloudSat is arguably the best spaceborne active sensor for global precipitation detection for the period studied.

### 2.3. Calculations of Back Trajectories

Back trajectories of the air parcels are calculated using the HYbrid Single Particle Lagrangian Integrated Trajectory Model (HYSPLIT; Draxler and Rolph, 2013) via the Air Resources Laboratory (ARL) of the National Oceanic and Atmospheric Administration (NOAA). In our case, the referenced meteorological data are obtained from the Global Data Assimilation System (GDAS). The ARL processes and archives this product as a 3-hourly, global, 1°×1° resolution data set on 21 prescribed pressure levels. The model was run in vertical motion mode and trajectories were initialized at locations where the mixed-phase clouds were observed by the aircraft. Calculations were performed at levels of 500, 1000, 2000 and 3000 m above sea level (a.s.l.), respectively. The initialization time for each level was the closest hour to the time that the aircraft was in mixed-phase clouds, and the total time-span of the trajectories calculated was 72 hours. In order to account for the uncertainties in the initial conditions, ensemble runs which include 26 additional trajectories were also performed. These runs were initialized at horizontal perturbations of one grid point, which is the standard configuration recommended by the ARL portal.

## 3. Observations and Analysis

### 3.1. Meteorology and Flight Overview

The mean sea level pressure (MSLP) analysis at 0600 UTC 07 Sep 2013 is shown in Figure 1(a). A cold front was approaching the southeast region of Australia, exposing Tasmania to the post-frontal air mass. Another cold front was travelling eastwards over the far south of the SO. The back trajectory calculations (Figure 2) reveal a south-westerly airstream with a long over-sea history, suggesting a pristine/baseline condition (Gras, 1995). There was an A-Train overpass at ~ 0425 UTC 07 Sep 2013 along the west coast of Tasmania. The MODIS true colour imagery (Figure 1b) reveals a widespread presence of a highly inhomogeneous open MCC cloud field over the vast post-frontal area. As the aircraft was restricted by Air Traffic

Control, our flight area was largely confined within a radius of ~ 100 nautical miles (~ 180 km) from Hobart Airport (-42.83°S, 147.50°E). As such, the flight path in this case was not in optimal alignment with the satellite ground track; nevertheless, the aircraft sampled the clouds within the nearest neighbourhood possible (~ 50 km east of the A-Train ground track) in order to optimize the comparison between the observations. An overview of the aircraft flight path overlaid on the MODIS cloud-top temperature image is shown in Figure 3(a). It is evident that the sampled clouds are largely representative of the cloud field in the broader post-frontal area, as observed by the satellites.

As noted previously, the geolocations, meteorological conditions, and cloud morphologies encountered during this flight are highly comparable to those examined in the previously mentioned study by Mossop et al. (1970).

### 3.2. In-situ Observations and Analysis

The time series of the in-situ measurements of thermodynamical and cloud microphysical properties for the whole flight are shown in Figure 4. The aircraft conducted a series of runs at a number of selected altitudes, with the central objective of sampling various parts of the clouds. The three segments where distinct cloud microphysical properties were measured are highlighted. Right before and after the cloud survey periods, two ~15-min airborne soundings (descent and ascent, respectively) were performed at ~ 1000 ft/min (~ 5 m/s) to document the thermodynamic structure of the atmosphere.

Temperature and wind profiles from the two airborne soundings (undertaken at ~ 0315 UTC and 0550 UTC, respectively) are shown in Figure 5. Both soundings were characterized by south-westerly winds at 7-10 ms$^{-1}$. The air mass in the lowest 2 km a.s.l. was neutrally stable and sub-saturated, indicative of shallow convection. No clear inversion was detected during the downward sounding (S1), whereas a saturated layer was observed with a capping temperature inversion (of about 5°C) during the upward sounding (S2). The soundings were performed within roughly the same geographical area, although S2 was ~ 50 km to the northeast of S1. Considering the fast-moving system with a wind speed of ~ 7-10 ms$^{-1}$ and soundings ~ 3 hours apart, it is estimated that S1 was slightly closer to the front compared to S2. This may partly explain the discrepancies seen in the profiles. Cloud-top temperatures (CTTs) from the two soundings and several other penetrations through the clouds during the flight varied between -6 and -9°C, largely in line with the MODIS CTTs over the broader area of the observations (Figure 3a).

The in-situ cloud microphysical properties differ considerably in the cloud samples penetrated by the two soundings. This does not exclude the possibility that the aircraft had exited through the side of what might actually be a deeper convective cell. During S1 (Figure 6, S1), a geometrically thin (~ 150 m) cloud sample with cloud top at ~ 1700 m (~ -6°C) was detected. This layer ('A') was observed to consist of "quasi-spherical" particles only (note that the digitization by the CIP limits the ability to determine with 100% accuracy if the particle is liquid or ice but that the quasi-spherical images at these temperature are most likely SLW), with $W_{liq(CAS)}$ and $N_{CAS}$ peaking at 0.8 g m$^{-3}$ and 100 cm$^{-3}$ near the cloud top (Figure 7, S1). The relatively high $N_{CAS}$ in this layer is further illustrated by the particle size distribution (PSD, Figure 8), which reveals a peak concentration (~ 100 cm$^{-3}$) at ~ 15 µm, suggesting a "pre-drizzle" state of these clouds. It is unlikely that ice shattering is making a noticeable contribution to the CAS concentrations since the CIP does not show any significant concentrations of crystals greater than 100 µm except in the lowest layer where the CAS concentrations are small. More drizzle-size particles were observed by the CIP as the aircraft continued to descend, accompanied with an increase in the particle size and decrease in liquid water content ('B' and 'C'). After a ~25s break, another thin layer was detected between 1.4 and 1.5 km a.s.l. at warmer temperatures (~ -3 to -4°C). This layer was, however, primarily mixed-phase ($\mu > 0.4$), with the CIP recording a large number of fresh ice crystals (column and hollow like habits) and few spherical particles (which were most likely supercooled drizzle) concurrently falling out of the cloud base. This layer is associated with a broadened distribution in the particle size spectrum, leading to the $N_{CIP}$ values being recorded up to 15 L$^{-1}$. The maximum lengths of the columnar ice crystals, according to the CIP, are typically within a range of 0.5-1.5 mm.

During S2, the observed cloud (CTTs ~ -9°C) was mostly dominated by supercooled drizzle-like particles (Figure 7, S2). No distinguishable ice-like particles were detected by the CIP during this penetration. $W_{liq(CAS)}$ and $N_{CAS}$ peaked at ~ 0.33 g m$^{-3}$ and 36 cm$^{-3}$, whereas $W_{liq(CIP)}$ and $N_{CIP}$ peaked at ~ 0.05 g m$^{-3}$ and 38 L$^{-1}$ (Figure 6, S2). Differing from S1, the PSDs from different layers of the clouds were more comparable, with an increase number of drizzle-size particles being detected towards cloud base (Figure 8). It is noted that $W_{liq(CAS+CIP)}$, $W_{liq(WCM\_021)}$ and $W_{liq(WCM\_083)}$ were rather consistent during S2, while $W_{TWC}$ was measurably higher than the other liquid water measurements. In fact, this discrepancy seems to be repeated throughout the entire flight. It is unclear why the $W_{TWC}$ values are systematically larger (at least in this presented case), although it could be speculated that this may in part be due to the scooped 4-mm total water probe being more efficient in collecting large precipitating particles than the cylindrical hot-wire liquid water probes, and/or the conservative estimate of liquid water content from the CIP measurements in heavy precipitation (see details in A4).

The cloud survey period is composed of three segments (Figure 4f). The first two segments (SEG-1 and SEG-2) were essentially an “in-cloud” survey where measurements were made at a fixed attitude of ~ 2 km, through approximately the middle of the cloud fieldbased on the observation during S1. The time series of the cloud microphysical properties during SEG-1 are shown in Figure 9. Note that the aircraft sampling was biased towards the larger cells that were considered to be most visible to the satellites. Due to an unexpected loss of communication with the air traffic control, there was a short break (~ 15 min, indicated in Figure 4a) between SEG-1 and SEG-2 where the aircraft had to make an ascent into clear air (at ~ 3.5 km a.s.l.) in order to resume communication. During SEG-1, two consecutive transects (~ 10-min each) were performed with reverse headings, whereby a well-defined convective cell (~ 2 km in diameter) was sampled twice, as reflected by the symmetric structure of the time series in Figure 9. The sampling was performed at ~ 1.8 km and between the -4 and -6°C isotherms. A closer examination reveals that the edges of this cloud cell (point ‘A’, ‘B’, ‘C’, ‘H’) were primarily liquid phase, where $W_{liq(CAS)}$, $W_{liq(WCM\_021)}$, and $W_{liq(WCM\_083)}$ were reasonably consistent, varying between ~ 0.8 and 1.2 g $m^{-3}$. Some heavily rimed particles were also captured (e.g. strip C and J in Figure 10). There was a sharp transition to the center of the cell (point ‘D’, ‘E’, ‘F’,' ‘G’), which was dominated by mixed phase and/or all ice, with fresh ice crystals being evident in the CIP images (Figure 10). The majority of the particle images were columns, some of which were rimed, covering a wide range of sizes. The $N_{CIP}$ was observed up to 40 $L^{-1}$ (with a 60-s average up to 18 $L^{-1}$) during SEG-1 in the cloud with $\mu$ e 0.9. A more conservative estimate of the ice number concentration with spherical particles (potentially water droplets) removed suggests a maximum of 26 $L^{-1}$ (with a 60-s average up to 15 $L^{-1}$) in this cloud. The differences in particle size characteristics in various parts of the cell can be better quantified with $r_{32}$ (Figure 9c), which showed a general increase when moving from the liquid-dominated to the ice-dominated part of the cell, with $r_{32(CAS)}$ increasing from ~ 12 to 15 μm, and $r_{32(CIP)}$ from ~

100 to 500 μm. The mean image area ratio (defined as the particle area divided by the area of the circumscribed circle) weighted by the count in each bin also changed from ~ 0.8 in the liquid-dominated to ~ 0.5 in the ice-dominated part, suggesting a transition from more spherical features to more non-spherical features. Cloud microphysical properties measured during SEG-2 (not shown) are very similar to those from SEG-1, despite some expected differences in the cell size of the sampled clouds. The $N_{CIP}$ was observed up to 54 $L^{-1}$ (with a 60-s average up to 14 $L^{-1}$) during SEG-2 (Figure 4c). The conservative estimate of the ice number concentration also reached 25 $L^{-1}$ (with a 60-s average up to 11 $L^{-1}$) in this segment.

Segment 3 (SEG-3) was an excursion where multi-level legs were flown at different altitudes – namely "above the sea surface (L1, ~ 200 m a.s.l.)", "below cloud base (L2, ~ 750 m a.s.l.)", "within clouds (L3, ~ 1400 m a.s.l.)", and "above cloud top (L4, ~ 2300 m a.s.l.)", as shown in Figure 11. Cloud cells sampled during SEG-3 were quite broken, with the horizontal dimensions (1-3 km) much smaller than those sampled during SEG-1 and SEG-2. Along L1 and L2 (point 'A', 'B' and 'C'), only large spherical particles were present in the CIP images (Figure 12), which were presumably raindrops. The $r_{32(CAS)}$ ($r_{32(CIP)}$) varied largely between ~ 9 and 14 μm (~ 200 and 600 μm). The CIP-derived instantaneous rain rate during L1 and L2 was calculated up to ~ 11 mm $h^{-1}$. The CIP-derived rain rate averaged at CloudSat resolution (1.7 km) was ~ 1.5 mm $h^{-1}$. The in-cloud measurements along L3 at ~ -4°C (point 'D', 'E' and 'F') were dominated by small SLW drops, with $r_{32(CAS)}$ reported in the range of 9-13 μm, and $r_{32(CIP)}$ being mostly below 150 μm. The in-cloud $N_{CAS}$ was in the range of 30-70 $cm^{-3}$, whereas $N_{CIP}$ was primarily below 12 $L^{-1}$. The conservative estimate of ice number concentration is very low, with a maximum of ~ 3 $L^{-1}$. The mean particle oblateness were generally greater than 0.7 in this segment. The CIP-derived instantaneous rain rate was up to 1.5 mm $h^{-1}$. There was little evidence of ice-like particles in the CIP images, although one of the images displays a few large, smooth ellipsoidal particles, which were likely to be rain drops. This may explain the non-zero values of the estimated ice number concentration.

In order to better appreciate the particle size characteristics, a composite of the normalized PSDs observed by the CAS and the CIP probes within the three segments is shown in Figure 13, for mixed-phase and liquid water dominated clouds, respectively. As noted, the mixed-phase clouds are generally characterized by higher number concentrations of larger particles and lower number concentrations of smaller particles, as opposed to the liquid water dominated clouds. Also, the PSDs measured from the CAS appear to be flatter for mixed-phase clouds, whereas a peak of the mean size centred at ~ 25 μm (corresponding to a mean number concentration of ~ 125 $cm^{-3}$) is noticed for liquid water dominated clouds. These characteristics seem to suggest an ice scavenging effect on the smaller liquid drops in the mixed-phase conditions, although a potential false response of the CAS in ice clouds cannot be ruled out.

### 3.3. Satellite Observations

The A-Train overpass was ~ 50 km upwind of the sampled area (Figure 3a). CloudSat traversed through a line of shallow convective cells, consistent with those sampled by the aircraft. Most of these clouds were precipitating, as suggested by the CPR reflectivities. Tthe maximum column radar reflectivity > -15 dBZ indicates precipitating clouds with a rain rate above ~ 0.02 mm $day^{-1}$ (Haynes and Stephens, 2007; Stephens et al., 2010). The maximum and average surface rain rates along the CloudSat track from 43 to 45°S were 8.1 and 0.21 mm $h^{-1}$, respectively, according to the CloudSat precipitation product. The ECMWF temperatures at cloud tops were ~ -4°C (slightly warmer than the measured CTTs), with a capping inversion present near cloud tops. The CALIPSO VFM product returns a range of categories. The aerosol classes were heavily dominated by "marine clean", although "polluted dust" was also infrequently reported. Note, however, that a known issue of the CALIPSO aerosol product is that the lidar ratio (defined as the extinction to backscatter ratio) that is used to determine aerosol subtypes is poorly characterized over a marine environment (e.g. Kiliyanpilakkil and Meskhidze, 2011). Measurements and model calculations show a wide range of lidar ratios (20-90 at the 532-nm channel) for clean marine aerosols. As such, there is a potential that the "polluted dust" (with lidar ratio typically of 55 ± 22) is simply a misclassification of coarse marine aerosols, such as sea spray. This issue is assessed with the back trajectory analysis presented in Section 3.4. The retrieved cloud phase was dominated by liquid (primarily SLW). "Unknown phase" and "ice phase" (including the class of "horizontally oriented ice") were also occasionally reported. Note that CALIOP is highly sensitive to small liquid water droplets that are present near cloud top, and that the VFM product does not include a "mixed phase" category. As such, when an "unknown" or "ice" phase is reported, we are almost certain that these clouds are primarily glaciated. The MODIS CPOP product, on the other hand, suggests a widespread presence of "liquid phase" clouds. "Ice phase" and "uncertain phase" are also reported, albeit much more sparsely. It is also interesting to note that the “non-liquid” cloud phases reported by the MODIS CPOP are generally close to the center of the cloud cells, which is similar to the in-situ observations. Focusing on the “liquid phase” clouds, the cloud droplet number concentrations estimated from the MODIS observations (using a modified version of the Bennartz (2007) method as used in Huang et al., (2016)) fall primarily in the range of 5-50 cm$^{-3}$ in the sample area, with notable inhomogeneity. Bearing our aircraft sampling bias in mind, both the CALIPSO and MODIS products seem to demonstrate reasonable consistencies with the in-situ cloud phase measurements. Despite these consistencies, it should be noted that the MODIS images of this case consist of a large number of “partly cloudy” or “cloud edge” pixels, which are considered to be poor candidates that suffer from large uncertainties or result in failed retrievals of some microphysical variables, such as effective radius and cloud optical thickness (Wolters et al., 2010; Zeng et al., 2012). Therefore, a detailed quantitative analysis/comparison of these properties with in-situ observations is not a focus for this case.

### 3.4. Air Mass History and Aerosol Properties

Figure 2 shows the ensembles of the back trajectories at various altitudes for the air mass sampled by the aircraft. The reliability of the vertical wind component can be problematic (e.g. Weller et al., 2014), especially for regions like the SO with sparse meteorological input data (Siems et al., 2000; Harris et al., 2005). Thus, in addition to the 3-D wind field, we also performed the calculations employing the isentropic approximation. The results (not shown) suggest that while the vertical profiles could differ significantly between the two approaches, the general horizontal advection characteristic appeared reasonably robust. Overall, the back trajectories suggest that the air mass over the lower troposphere of the SO can be characterized by cold air advection, with a pristine/baseline air mass for well over 72 hours. The air was weakly descending below 2 km and showed very little spread between the ensemble members. In general, we see little (if any) signature of long-range transport of continental aerosols from the 72-hour trajectories, suggesting that the majority of the aerosols are likely of marine origin. This is consistent with recent studies suggesting that marine organic material may be an important source of INP over the SO (e.g. Wilson et al., 2015; DeMott et al., 2016).

While it is not possible to directly infer any potential ice-nucleating particles and their number concentrations from our limited in-situ observations, it may be reasonable to expect that the INP active warmer than -10°C is very scarce, given the pristine nature of the air mass. It has been reported in the literature that the INP concentrations over the SO are notably low, typically in a range of 0.01- 0.1L$^{-1}$ at temperatures below -15°C (e.g. Bigg, 1973; Burrows et al., 2013; Wilson et al., 2015). Given that the CAS measures particle size down to ~ 0.6 μm, which is the upper tail of the accumulation mode aerosols and giant nuclei, it is useful to examine the aerosol properties measured by the CAS in clear air (defined as $W_{TWC}$ < 0.01 g m$^{-3}$) and below and above cloud, as these aerosols are potential cloud condensation nuclei (CCN) and INP. DeMott et al. (2010, hereafter D10) proposed an INP parameterization scheme which incorporates both aerosols and temperatures to estimate INP concentrations. The relation is expressed as:

$$N_{INP,T_k} = a(273.16 - T_k)^b (N_{aer,0.5})^{(c(273.16-T_k)+d)} \quad (2)$$

where a=0.0000594, b=3.33, c=0.0264, d=0.0033, $T_k$ is cloud temperature in degree Kelvin, $N_{aer,0.5}$ is the number concentration (cm$^{-3}$) of aerosol particles with diameters larger than 0.5 μm, and $N_{INP,Tk}$ is the estimated INP number concentration (L$^{-1}$) at $T_k$. The D10 parameterization requires a concentration of aerosol particles with diameters greater than 0.5 μm ($N_{aer,0.5}$) as they suggest that INP particles are most commonly observed within this size range. D10 further suggests that this scheme outperforms older parameterizations that are based on temperature alone. Grosvenor et al. (2012) also employed the D10 parameterization to estimate the INP concentrations using in-situ measurements over Antarctica, finding that the estimates with this scheme compared the most favourably with the observations at heterogeneous ice formation temperatures. Following Grosvenor et al. (2012), we use the aerosol concentration above 0.6 μm measured by the CAS as a surrogate for the $N_{aer,0.5}$ parameter for the INP estimations. We also apply an upper limit of 2 μm while the maximum possible sampled aerosol size in D10 was 1.6 μm. This is a compromise as an exact match of the size range is not possible given the channels available from the CAS.

The clear air $N_{aer,0.5}$ measured by the CAS and the associated INP concentrations ($N_{INP,\ Tk}$) estimated with the D10 scheme are shown for the two soundings in Figures 6(e) and (j). Overall, the clear air $N_{aer,0.5}$ below cloud base is within the range of 1-10 cm$^{-3}$, while the values drop down to 0.01-0.1 cm$^{-3}$ above cloud. The aerosol profiles in the boundary layer are comparable for the two soundings, whereas the $N_{aer,0.5}$ concentrations immediately above the cloud are higher during S1. Accordingly, the estimated $N_{INP,Tk}$ is estimated to be within a range of 10$^{-5}$-10$^{-1}$ L$^{-1}$ (at temperatures of -6 to 0°C) in the boundary layer and 10$^{-2}$-10$^{-1}$ L$^{-1}$

above cloud (at temperatures of -9 to -6°C). These estimated values are largely consistent with those reported in the literature over the SO (e.g. Bigg 1973; Burrows et al. 2013; Wilson et al. 2015). The $N_{aer,0.5}$ and $N_{INP,Tk}$ in clear air within the three segments are also examined (not shown). Overall, the values are consistently low. The $N_{aer,0.5}$ and $N_{INP,Tk}$ values are largely below 3 $cm^{-3}$and $10^{-1}$ $L^{-1}$(at temperatures between -10 and -5°C), respectively.

It should be noted that sea salt aerosols may contribute significantly to the aerosol total numbers for particle sizes greater than 0.5 μm in the marine boundary layers (O'Dowd et al., 1997; D10). However, sea salt aerosols are not known to have any role in ice nucleation in the temperature range we considered (D10). As such our $N_{aer,0.5}$ may be an overestimate. Also, measurements immediately below or above cloud were often accompanied by high relative humidity, in which case the $N_{aer,0.5}$ may be overestimated due to swelling effects of smaller aerosols. On the other hand, the CAS probe cannot measure particle sizes between 0.5 and 0.6 μm, meaning that our $N_{aer,0.5}$ may tend towards an underestimate, compared to what would be expected if measurements within this size range were available. All these uncertainties contribute to the difficulties of measuring $N_{aer,0.5}$ and may have an compensating effect on the overall error of the estimations.

### 3.5. Extended Analysis of Air Mass History

In addition to the observations presented above, it is possible to extend the back trajectory calculation to further explore the history of the air mass and associated cloud properties. This analysis is assisted with two additional A-Train overpasses occurring ~ 23 and ~ 46 hours upwind of the in-situ measurements (Figure 2a), based on the back trajectory calculations. Retrieved cloud properties of these two overpasses are shown in Figure 14 and 15, respectively. The most immediate feature, as shown in the MODIS imagery (Figure 14a and 15a), is a transition from a closed MCC cloud field to a widespread open MCC cloud field, as the air mass travels east and northwards. The stratiform clouds were preferentially present over colder sea surface temperatures (SSTs, SST < 4°C) with much weaker SST gradients (Figure 14c and 15c), while the broken cumulus clouds were typically found over warmer SSTs, with the break-up starting at regions where relatively strong SST gradients were present. The transition in the cloud morphology is further accompanied with a similar pattern in the cloud phase transition (Figure 14b and 15b). The stratiform clouds were dominated by SLW within the temperature range of -10 to -20°C, whereas the open MCC clouds were dominated by a mix of "liquid", "ice" and "uncertain" phase that were intermittently distributed (note that a "mixed phase" category is not produced by the MODIS standard cloud product in collection 6). The open MCC cloud morphology is similar to that present in Figure 3, albeit the ambient temperatures were generally colder at higher latitudes.

During these two A-Train overpasses, CloudSat and CALIPSO only traversed the open MCC cloud fields, which were, once again, precipitating, as suggested by the CPR (Figure 14d and 15d). The CloudSat maximum and average surface rain rates along the track on 06 Sep were 19.7 and 0.7 mm $h^{-1}$, respectively. The surface rain rate was not available for the overpass on 05 Sep as the precipitation was diagnosed as mixed phase for which the surface rain rate was not produced by the CloudSat algorithms. For both cases, cloud tops were observed up to ~ 3 km. CALIPSO phase categorizations (Figure 14e and 15e) are largely consistent with the MODIS CPOP retrievals. Ice was reported in appreciable quantities in the widespread (up to thousands of kilometres) open-cellular cloud fields in the temperature range of -5 to -15°C, according to both MODIS and CALIPSO products. While some cirrus clouds were also detected by CALIPSO above 4 km, the fractional cover is small (49-51°S in Figure 14e and 50-52°S in Figure 15e). Thus, it is unlikely that the ice observed at the lower altitudes could be explained by a classic "seeder-feeder" effect, where the lower-level liquid clouds are seeded by the ice crystals falling out of the overlying cirrus.

Overall, the analysis of the air mass history suggests that: (1) the open MCC clouds have been tracked over 46 hours with A-Train observations and the presence of these clouds is common over the SO during this period of time, and (2) according to the satellite observations, the open MCC, which is commonly present as mixed-phase clouds, tends to form preferentially over strong SST gradients (more unstable environment), while the closed MCC (stratiform clouds), which is often present as SLW clouds, tends to form over the colder ocean with weak SST gradients (more stable environment).

## 4. Discussions

The ice number concentrations observed from the aircraft measurements were one to three orders of magnitude larger than the INP number concentrations ($N_{INP,Tk}$) estimated with the D10 parameterization scheme and in comparison with the values typically reported in the literature over the remote SO region. Considering the low $N_{INP,Tk}$ values, the uncommonly high ice number concentration measured by the aircraft and little evidence of a classic "seeder-feeder" mechanism, it is not unreasonable to speculate that the high ice number concentrations observed in such a warm temperature range is produced via a secondary ice mechanism, as originally proposed by Hallett and Mossop (1974) and the follow-on studies.

As discussed before, the H-M mechanism is the most widely studied and quantified secondary ice production mechanism, among several others (each with different required conditions). The H-M is known to be active in the temperature range of -3 to -8°C, and requires the presence of graupel and cloud droplets smaller than 13 μm and drops larger than 24 μm in diameter. Also, an expected product of H-M is the large concentrations of columnar ice crystals. As shown in Figure 8, droplets sizes within the required ranges were observed in reasonable quantities during the flight. In addition, columnar ice crystals were observed to be ubiquitous in the glaciated regions (Figure 10). Given that all these known conditions were met, it was likely that the secondary ice production was actively operating via the H-M pathway.

To quantitatively assess whether the H-M process could be responsible for the large number concentrations of ice particles observed by the aircraft, we adopt the approach of Harris-Hobbs and Cooper (1987, hereafter HC87) to estimate the splinter production rate. To do this, ice crystal size distribution, measured with the CIP measurements in the vicinity of the H-M region during SEG-1 and 2 were used. Following HC87, we restrict our analysis to crystals whose sizes are within the range of 62.5-162.5 μm (taking into account the available CIP channels) to avoid effects of nearby droplets on crystal growth rates at large crystal sizes and to minimize the corrections for variable depth-of-field. Assuming that ice particles constantly grow in a water saturated environment, these crystals would have a linear growth rate of ~ 1.4 μm s$^{-1}$ at ~ -6°C (as described by Ryan et al., 1976). Accordingly, the time required for crystals to grow from 62.5 to 162.5 is (162.5-62.5) μm /1.4 μm s$^{-1}$ = 71.4 s (equation (5) in HC87). If we assume that ice splinters are the only source of ice crystals moving through this size range, then the splinter production rate is *´N/Ä*(equation (4) in HC87), where *´N* is the number concentration of crystals in the size range of 62.5-162.5 μm and *Ä*is the time taken for the ice crystals moving through this size range (i.e. 71.4 s). In our case, *´N/Ä*is calculated to be in the range of 30-70 m$^{-3}$ s$^{-1}$. This result is largely consistent with the splinter production rate measured in Crosier et al. (2011), where ice multiplication was observed in a weakly convective cell embedded in supercooled mid-level stratus over the UK. As described in Section 3.2, the evidence of ice multiplication was observed at ~ 2 km (Figures 4 and 9), which was ~ 0.4 km above the cloud base (Figure 6). If we assume that the ice multiplication occurred in a weakly convective condition with an updraft of 1 m $s^{-1}$, with the calculated splinter production rate of 30-70 $m^{-3}$ $s^{-1}$, the ice number concentration that should be reached at 2 km is calculated to be in a range of 10-30 $L^{-1}$. This is comparable to the range of the ice number concentrations observed in the H-M zone, which suggests that the observed ice number concentrations in our case are largely consistent with the theoretical calculations where the ice crystals are assumed to be produced via a splinter production.

Moving beyond the ice multiplication, it is unclear why there was such a large contrast between S1 and S2, and between SEG-1 and SEG-3 in terms of the observed cloud phase compositions. It is possible that the evolution of the air mass during the flight might have a fundamental impact; however the lack of vertical velocity measurements prohibits a more quantifiable explanation. Cloud age may be another key controlling factor: it is likely that the liquid clouds sampled during S2 and SEG-3 (within the H-M temperature range) had already experienced precipitation (i.e. they were at a "post-precipitation" state), given their low, in-cloud $N_{CAS}$ values. In contrast, the mixed-phase clouds sampled in S1 and SEG-1 might be evolving towards a mature state. Unfortunately, direct observations that could be used to assist an estimate of the cloud age were unavailable in our case.

## 5. Concluding Remarks

Uncommonly high number concentrations (up to 54 $L^{-1}$) of ice particles present in cloud temperatures warmer than -9°C were encountered by an instrumented Cessna Conquest aircraft over the Southern Ocean (SO), off the southwest coast of Tasmania, Australia. The observed ice number concentrations were one to three orders of magnitude larger than the INP number concentrations estimated with an ice nuclei parameterization scheme and the values typically reported in the literature over this remote region. The sampled cloud field was characterized by open-cellular, shallow convection, present in a large-scale environment defined as cold air advection, with a pristine/baseline air mass for well over 72 hours. The open cellular clouds were observed to be precipitating. Satellite observations from an A-Train overpass in the near neighborhood during the flight period reveal a qualitatively consistent story, with the presence of mixed-phase (but predominantly SLW) clouds with cloud-top temperatures at ~ -6°C. Further analysis of the air mass history shows that ice particles found in a relatively warm temperature range could potentially exist in appreciable quantities, within the widespread (up to thousands of kilometers) shallow convective cloud fields over the SO.

Although the lack of in-situ measurements of simultaneous ice, droplet, INP and aerosol composition was a significant limiting factor for a detailed study on cloud microphysics, the direct in-situ evidence of ice particles in uncommonly high number concentration is remarkable, given the pristine nature of the air mass over this region and the low INP concentrations we estimated and typically reported in the literature. The hypothesis that the poor representation of SLW contributes substantially to the simulated cloud and radiative biases in climate models over the SO (e.g. Bodas-Salcedo et al., 2016; McCoy et al., 2015) has gained increasing traction over the past years. Yet a comprehensive understanding of the formation and persistence of SLW is still lacking. An open question remains as to the conditions and extent (e.g. spatiotemporal variability) under which SLW dominates the mixed-phase clouds and precipitation in the SO. The presented case suggests that secondary ice production (likely the H-M process) has the potential to be commonplace in the remote, pristine SO. It is interesting to note that the integral story of these findings is in broad agreement with the in-situ measurements obtained from the Antarctic Peninsula and Larsen Ice Shelf, where high ice concentrations are commonly observed in the H-M temperature range and SLW is more frequently encountered at colder temperatures (Grosvenor et al., 2012).

It is intriguing to note that, qualitatively, the A-Train satellite products seems to demonstrate some skill in observing the microphysical nature of the SO clouds that compare favourably with the in-situ measurements. The A-Train observations tracked over 23 and 46 hours prior to the in-situ observations show that  a link is present between the mesoscale cloud morphologies (e.g. cellularity) and the fine-scale cloud microphysics (e.g. cloud phase). As such, these satellite observations offer the potential for a climatological description of secondary ice production with respect to seasonality, cloud type (particularly for shallow convective clouds given their prevalence), cloud depth, and the development of precipitation over the SO. A better understanding and characterization of precipitation processes of these clouds is necessary for closing the water and energy budget in this climatically important region.

Despite the preliminary nature of this study, our analysis ties in with the early proposal of the H-M mechanism over the SO (Hallett and Mossop, 1974; Mossop and Hallett, 1974; Mossop, 1976), and reinforces the role of secondary ice production that may potentially be important in clouds and precipitation development in this region. We propose three key questions that should be the focus of future research: (1) what is the source of INP for these clouds, (2) why aren't these INP present at higher elevations/colder temperatures where solid SLW layers have been observed previously (e.g. Chubb et al. 2013; Grosvenor et al. 2012), and (3) how important are (warm) ice processes for the development of precipitation in these clouds? Dedicated field campaigns with multi-observational and instrumental platforms are critical to address these outstanding questions.

# Appendix

## A1. CAPS Measurements and Uncertainties

The measurement uncertainties and limitations of light scattering and imaging spectrometers, such as the CAS and the CIP, respectively, have been evaluated in many studies and are summarized in the book by Wendisch and Brenguier (2014) and a new monograph to be published by the American Meteorological Society (Baumgardner et al., 2016). The sizing accuracy of the CAS is ±20% for water droplets and ±30% when measuring ice crystals. The uncertainty in number concentration is ±15% when measuring < 300 $cm^{-3}$. The root sum squared error in derived liquid water content is 38% and 54% for ice water content. The CIP sizing accuracy is the same for droplets or ice crystals, but varies with size, with an average uncertainty of 25%. The concentration uncertainty is also size dependent but is also on average estimated to be 20%. The largest uncertainties are for particles < 100 μm because of particles that are detected but are out of focus and whose images are larger than the physical size. This can produce as much as a 50% positive bias. The propagated error in derived liquid/ice water content is ±48%; however, this does not account for the uncertainties in the assumed volume and density of ice crystals.

## A2. SEA WCM-2000 Measurements and Uncertainties

Unlike the CAPS, the SEA WCM-2000 is a relatively new probe that has not received the same level of scrutiny. This instrument is designed to minimize the issues that the older model hotwire probes have, i.e. decreased sensitivity for larger droplets (Biter et al., 1987; Strapp et al., 2003) and the response of the liquid water content sensor to ice crystals (Cober et al., 2001). Although Lilie et al. (2005) show wind tunnel measurements that suggest that the WCM-2000 does not roll off until much larger drop sizes than other hotwire instruments; it is very likely that the WCM-021 sensor will respond to ice crystals similar to the hotwire with the same dimension. This means that in mixed-phase clouds, the separation between liquid and solid phase may still be biased.

## A3. Calculations of $W_{ice}$ and $W_{liq}$ from WCM-2000 Measurements

Following Korolev et al. (2003, K03), $W_{ice}$ (ice water content) and $W_{liq}$ (liquid water content) are calculated using equations (A1) and (A2) below

$$W_{TWC} = \mathcal{E}_{liqT} W_{liq\,(WCM)} + k\mathcal{E}_{iceT} W_{ice\,(WCM)} \quad \text{(A1)}$$

$$W_{LWC(083)} = \mathcal{E}_{liqL} W_{liq\,(WCM)} + \beta W_{ice\,(WCM)} \quad \text{(A2)}$$

where $W_{TWC}$ and $W_{LWC\,(083)}$ are the total- and liquid-water contents measured by the WCM-2000 total water and liquid water (2-mm) sensors, respectively; $\mathcal{E}_{liqT}$ and $\mathcal{E}_{iceT}$ are the integrated collection efficiencies of liquid and ice particles for the total water sensor; $\mathcal{E}_{liqL}$ is the integrated collection efficiency for liquid droplets for the liquid water sensor; $\beta$ is the coefficient accounting for the residual effect of the ice on the liquid water sensor; $k$ is the correction coefficient for the difference between expended specific energy of water evaporation and ice sublimation. Following K03, we assume $\mathcal{E}_{liqT}$, $\mathcal{E}_{iceT}$ and $\mathcal{E}_{liqL}$ to be unity. $k$ is calculated from equation (5) and (6) in K03, which is 1.12. $\beta$ is estimated to be 0.142, which is derived from a number of other flights in our project when measurements were made in clouds with temperatures < -25°C, where the observed clouds are assumed to be completely glaciated. Note that the value of $\beta$ may vary in different types of clouds, due to the differences in the size, habits and bulk density of particles.

### A4. CIP Data Processing

Particle images from CIP measurements are processed with the ‘SODA’ program (version 2) developed by the US National Center of Atmospheric Research. To determine the CIP number concentration, the calculation of sample volume is important. The mathematical expression of the CIP sample volume (SV) is given by equation (A3):

$$SV = SA \times v \times t \quad \text{(A3)}$$

where SA is the sample area, *v* is the probe speed which has been synchronized with the true air speed (TAS) in our case, *t* is the sampling time. The sample area (SA) is the product of the depth of field (DOF, defined as the length along the laser beam) and the effective array width (EAW, defined as the width of the sample area perpendicular to the DOF and air flow. In our study, the 'center-in' technique (Heymsfield and Parrish, 1978) is used for calculating the sample area. The ‘centre-in’ technique is preferable for quasi-symmetric or symmetric particles like raindrops, graupel, hail, dendrites and rimed aggregates whose centers are located within the detector array.

To minimize the sampling uncertainties, cloud particles that are not properly imaged are rejected (Korolev, 2007; Heymsfield and Parrish, 1978), using a number of the built-in functions within the program. The default rejection criteria are: (1) Area ratio < 0.1; (2) particle size outside of measurement size range. The area ratio is defined as the shaded particle area divided by the area covered by the area of a circumscribed circle (McFarquhar and Heymsfield, 1996). It gives a measure of the sphericity of a particle, which gives an indication of particle phase. Most liquid phase particles have area ratios > 0.8. Given the relatively large uncertainties associated with the measurements from the first couple of bins, we specify the starting bin size at 62.5 μm for all the computations. Therefore, ice and liquid water concentrations are only counted for particles that are larger than this size, which means that newly nucleated ice particles may be undetected in this study. However, in mixed phase clouds ice particles grow rapidly, which means that they should become detectable fairly quickly (commonly in a falling distance of ~ 90 m, as suggested by Mitchell and Heymsfield, 2005). For more reliable sizing, larger bin sizes are used (by combining several bins with the natural resolution) to get sufficient particle counts in each bin.

Large particles that impact on the forward surface of a probe arm can break into many pieces and then be imaged by the probe. This could result in an overestimate of the concentration of small particles. To estimate the total number concentration ($N_{CIP}$), a "shattering correction" (Field et al., 2006) is applied to identify and remove any artefacts. The basis of the algorithm is a bimodal Poisson probability density function that describes the distribution of interarrival time (Ä); where particles occurring in a peak with a larger mode Ä$_1$ correspond to naturally occurring particles and those in a peak with a smaller mode Ä$_2$ correspond to shattered particles. The algorithm uses a flexible cutoff depending on the overall particle concentration for the processed time period. Further elaboration and analysis of limitations of the interarrival time algorithm is described in Korolev and Field (2015) and an overview of the algorithms available for shattering correction is provided in the monograph by McFarquhar et al. (2016). It is suggested that there has been no general consensus currently on the superiority of any algorithms. As such, differences in observed size distributions are expected depending on the approaches used. Nevertheless, we expect the "shattering correction" and the default rejection criteria to be able to reject most of the shattered artefacts. . To estimate liquid water content with the CIP, stricter processing criteria are applied, which include: (1) "all-in" – only particles that are fully imaged and do not touch an edge of the array are examined; (2) "water processing" – stricter roundness criteria is applied to limit processing to particles that may be liquid water, including the Korolev (2007) size correction which reduces the size of the“out of focus” images, particles with (a) area ratio < 0.4, (b) area ratio < 0.5 and occupying 10 pixels or larger, (c) size greater than 6 mm, and (d) corrected particle size outside of size-bin range are rejected; (3) “stuck bit correction” – only looking for diodes that are either continuously on or continuously off and correct for the errors by using neighbouring diodes.

## Acknowledgements

This research was funded by ARC discovery grant DP150102894. We greatly appreciate Aaron Bansemer from the US National Center for Atmospheric Research for providing support with the SODA-2 software.

## Reference

Ackerman AS, Toon OB, Hobbs PV. 1993. Dissipation of marine stratiform clouds and collapse of the marine boundary layer due to the depletion of cloud condensation nuclei by clouds. *Science*. **262** (5131): 226-229, doi:10.1126/science.262.5131.226.

Atkinson BW, Zhang JW. 1996. Mesoscale shallow convection in the atmosphere. *Rev. Geophys.* **34**: 403–431.

Avramov A, Ackerman AS, Fridlind AM, van Diedenhoven B, Botta G, Aydin K, Verlinde J, Korolev AV, Strapp JW, McFarquhar GM, Jackson R, Brooks SD, Glen A, Wolde M. 2011. Toward ice formation closure in Arctic mixed-phase boundary layer clouds during ISDAC. *J. Geophys. Res.* **116**: D00T08, doi:10.1029/2011JD015910.

Bacon N, Swanson B, Baker M, Davis E. 1998. Breakup of levitated frost particles. *J. Geophys. Res.* **103**: 13763-13775, doi:10.1029/98JD01162.

Bates TS, Huebert BJ, Gras JL, Griffiths FB, Durkee PA. 1998. International global atmospheric chemistry (IGAC) project's first aerosol characterization experiment (ACE 1): overview. *J. Geophys. Res.* **103**(D13): 16297-16318, doi: 10.1029/97JD03741.

Baumgardner D, Jonsson H, Dawson W, O'Connor D, Newton R. 2001. The cloud, aerosol and precipitation spectrometer: A new instrument for cloud investigations. *Atmos. Res.* 59–60, 251–264.

Beard K. 1992. Ice initiation in warm-base convective clouds: An assessment of microphysical mechanisms. *Atmos. Res.* **28**: 125-152.

Bigg EK. 1973. Ice nucleus measurements in remote areas. *J. Atmos. Sci.* **30**: 1153-1157.

Biter CJ, Dye JE, Huffman D, King WD. 1987. The dropsize response of the CSIRO liquid water probe. *J. Atmos. Oceanic Technol.* **4**: 359–367.

Bodas-Salcedo A, Hill PG, Furtado K, Williams KD, Field PR, Manners JC, Hyder P, Kato S. 2016. Large contribution of supercooled liquid clouds to the solar radiation budget of the Southern Ocean. *J. Clim.* **29**(11): 4213-4228, doi: 10.1175/JCLI-D-15-0564.1.

Boers R, Jensen JB, Krummel PB. 1998. Microphysical and short-wave radiative structure of marine stratocumulus clouds over the Southern Ocean: Summer results and seasonal differences. *Quart. J. Roy. Meteor. Soc.* **124**: 151-168.

Burrows SM, Hoose C, Pöschl U, Lawrence MG. 2013. Ice nuclei in marine air: Biogenic particles or dust? *Atmos. Chem. Phys.* **13**: 245-267, doi:10.5194/acp-13-245-2013.

Cantrell W, Heymsfield A. 2005. Production of Ice in Tropospheric Clouds: A Review. *Bull. Am. Meteorol. Soc.* **6**: 975-807, doi: http://dx.doi.org/10.1175/BAMS-86-6-795.

Chubb TH, Jensen JB, Siems ST, Manton MJ. 2013. In-situ observations of supercooled liquid clouds over the Southern Ocean during the HIAPER Pole-to-Pole Observation campaigns. *Geophys. Res. Lett.* **40**: 5280-5285, doi:10.1002/grl.50986.

Cober SG, Isaac GA, Korolev AV, Strapp JW. 2001. Assessing cloud-phase conditions. *J. Appl. Meteorol.* **40**(11): 1967–1983.

Cooper WA. 1986. Ice initiation in natural clouds. Precipitation enhancement - A scientific challenge. *Meteor Monogr*. **21**: 29-32.

Crosier J, Bower KN, Choularton TW, Westbrook CD, Connolly PJ, Cui ZQ, Crawford IP, Capes GL, Coe H, Dorsey JR, Williams PI, llingworth AJ, Gallagher MW, Blyth IP. 2011. Observations of ice multiplication in a weakly convective cell embedded in supercooled mid-level stratus. *Atmos. Chem. Phys.* **11**: 257–273.

DeMott PJ, and coauthors. 2010. Predicting global atmospheric ice nuclei distributions and their impacts on climate. *Proc. Natl. Acad. Sci.* **107**(25): 11217-11222.

DeMott PJ, and coauthors. 2016. Sea spray aerosol as a unique source of ice nucleating particles. *Proc. Natl. Acad. Sci.* **113**(21): 5797-803.

Dong X, Mace GG. 2003. Arctic stratus cloud properties and radiative forcing derived from ground-based data collected at Barrow, Alaska. *J. Clim.* **16**: 445-461.

Draxler RR, Rolph GD. 2013. HYSPLIT (HYbrid Single-Particle Lagrangian Integrated Trajectory) Model access via NOAA ARL READY Website (http://ready.arl.noaa.gov/HYSPLIT.php), NOAA Air Resources Laboratory, Silver Spring, Md.

Ellis TD, L'Ecuyer T, Haynes JM, Stephens GL. 2009. How often does it rain over the global oceans? The perspective from CloudSat. *Geophys. Res. Lett.* **36**: L03815, doi:10.1029/2008GL036728.

Field PR, Hogan RJ, Brown PRA, Illingworth AJ, Choularton TW, Kaye PH, Hirst E, Greenaway R. 2004. Simultaneous radar and aircraft observations of mixed-phase cloud at the 100-m scale. *Q. J. R. Meteorol. Soc.* **130**: 1877-1904.

Field PR, Heymsfield AJ, Bansemer A. 2006. Shattering and particle interarrival times measured by optical array probes in ice clouds. *J. Atmos. Ocean. Technol.* **23**: 1357-1371, doi:10.1175/JTECH1922.1.

Field PR, Wood R. 2007. Precipitation and cloud structure in mid-latitude cyclones. *J. Clim.* **20**: 233–254.

Field PR, Lawson R, Brown P, Lloyd G, Westbrook C, Moisseev D, Miltenberger A, Nenes A, Blyth A, Choularton T, Connolly P, Buehl J, Crosier J, Cui Z, Dearden C, DeMott P, Flossmann A, Heymsfield A, Huang Y, Kalesse H, Kanji Z, Korolev A, Kirchgaessner A, Lasher-Trapp S, Leisner T, McFarquhar G, Phillips V, Stith J, Sullivan S. 2016. Chapter 7. Secondary Ice Production - current state of the science and recommendations for the future. *Meteor. Monogr.* doi:10.1175/AMSMONOGRAPHS-D-16-0014.1, in press.

Gras JL. 1995. CN, CCN and particle size in Southern Ocean air at Cape Grim. *Atmos. Res.* **35**: 233-251, doi:10.1016/0169-8095(94)00021-5.

Grosvenor DP, Choularton TW, Lachlan-Cope T, Gallagher MW, Crosier J, Bower KN, Ladkin RS, Dorsey JR. 2012. In-situ aircraft observations of ice concentrations within clouds over the Antarctic Peninsula and Larsen Ice Shelf. *Atmos. Chem. Phys.* **12**: 11275-11294, doi:10.5194/acp-12-11275-2012.Hallett J, Mossop S. 1974. Production of secondary ice crystals during the riming process. *Nature*. **249**: 26-28.

Harris-Hobbs R, Cooper W. 1987. Field evidence supporting quantitative predictions of secondary ice production rate. *J. Atmos. Sci.* **44**: 1071-1082.

Harris JM, Draxler RR, Oltmans SJ. 2005. Trajectory model sensitivity to differences in input data and vertical transport method. *J. Geophys. Res.* **110**: D14109, doi:10.1029/2004JD005750.

Haynes JM, Stephens GL. 2007. Tropical oceanic cloudiness and the incidence of precipitation: Early results from CloudSat. *J. Geophys. Res.* **34**: L09811, doi:10.1029/2007GL029335.

Heymsfield AJ, Parrish JL. 1978. A computational technique for increasing the effective sampling volume of the PMS two-dimensional particle size spectrometer. *J. Appl. Meteorol.* **17**: 1566–1572.

Heymsfield A, Willis P. 2014. Cloud conditions favouring secondary ice particle production in tropical maritime convection. *J. Atmos. Sci.* **71**: 4500-4526.

Hobbs PV, Rangno AL. 1985. Ice particle concentrations in clouds. *J. Atmos. Sci.* **36**: 2523-2549.

Hobbs PV, Rangno AL. 1990. Rapid development of ice particle concentrations in small polar maritime cumuliform clouds. *J. Atmos. Sci.* **47**: 2710-2722.

Hogan RJ, Field PR, Illingworth AJ, Cotton RJ, Choularton TW. 2002. Properties of embedded convection in warm-frontal mixed-phase cloud from aircraft and polarimetric radar. *Quart. J. Roy. Meteorol. Soc.* **128**: 451-476.

Hu Y, and Coauthors. 2009. CALIPSO/CALIOP cloud phase discrimination algorithm. *J. Atmos. Oceanic Technol.* **26**: 2293-2309, doi:10.1175/2009JTECHA1280.1.

Hu Y, Rodier S, Xu K, Sun W, Huang J, Lin B, Zhai P, Josset D. 2010. Occurrence, liquid water content, and fraction of supercooled water clouds from combined CALIOP/IIR/MODIS measurements. *J. Geophys. Res.* **115**: D00H34, doi:10.1029/2009JD012384.

Huang Y, Si

Huang Y, Siems ST, Manton MJ, Hande LB, Haynes JM. 2012b. The structure of low-altitude clouds over the Southern Ocean as seen by CloudSat. *J. Clim.* **25**: 2535–2546, doi: 10.1175/JCLI-D-11-00131.1.Huang Y, Franklin CN, Siems ST, Manton MJ, Chubb T, Lock A, Alexander S, Klekociuk A. 2015. Evaluation of boundary-layer cloud forecasts over the Southern Ocean in a limited-area numerical weather prediction system using in-situ, space-borne and ground-based observations. *Quart. J. Roy. Meteorol. Soc.* **141**: 2259-2276, doi:10.1002/qj.2519.

Huang Y, Siems ST, Manton MJ, Rosenfeld D, Marchand R, McFarquhar GM, Protat A. 2016. What is the role of sea surface temperature in modulating cloud and precipitation properties over the Southern Ocean? *J. Clim.* **29**: 7453–7476, doi: 10.1175/JCLI-D-15-0768.1.

Kiliyanpilakkil VP, Meskhidze N. 2011. Deriving the effect of wind speed on clean marine aerosol optical properties using the A-Train satellites. *Atmos. Chem. Phys.* **11**: 11401-11413, doi:10.5194/acp-11-11401-2011.

Korolev A, Isaac GA, Cober SG, Strapp JW, Hallett J. 2003. Microphysical characterization of mixed-phase clouds. *Q. J. R. Meteorol. Soc.* **129**: 39-65.

Korolev A, Isaac GA. 2005. Shattering during sampling by OAPs and HVPS. Part I: Snow particles. *J. Atmos. Technol.* **22**: 528-542, doi:10.1175/JTECH1720.1.

Korolev A. 2007. Reconstruction of the Sizes of Spherical Particles from Their Shadow Images. Part I: Theoretical Considerations. J. Atmos. Oceanic Tech. 24:376-389, doi: 10.1175/JTECH1980.1.

Korolev, AV, Emery, EF, Strapp, JW, Cober, SG, Isaac, GA, Wasey, M, Marcotte, D. 2010. Small ice particles in tropospheric clouds: fact or artifact? Airborne Icing Instrumentation Evaluation Experiment, doi:10.1175/2010BAMS3141.1.

Korolev AV, Emery EF, Strapp JW, Cober SG, Isaac GA, Wasey M, Marcotte D. 2011. Small ice particles in tropospheric clouds: Fact or artifact? *Bull. Amer. Meteor. Soc.* **92**: 967-973, doi:10.1175/2010BAMS3141.1.

Korolev A, Field PR. 2015. Assessment of the performance of the inter-arrival time algorithm to identify ice shattering artifacts in cloud particle probe measurements. *Atmos. Meas. Tech.* **8**: 761–777.

Lawson RP. 2011. Effects of ice particles shattering on the 2D-S probe. *Atmos. Meas. Tech.* **4**: 1361-1381, doi:10.5194/amt-4-1361-2011.

Mace GG, Marchand R, Zhang Q, Stephens G. 2007. Global hydrometeor occurrence as observed by Cloudsat: Initial observations from summer 2006. *Geophys. Res. Lett*. **34**: L09808, doi:10.1029/ 2006GL029017.

McCoy DT, Hartmann DL, Zelinka MD, Ceppi P, Grosvenor DP. 2015. Mixed-phase cloud physics and Southern Ocean cloud feedback in climate models. *J. Geophys. Res.* **120** (18): 9539-9554.

McFarquhar GM, Heymsfield AJ. 1996. Microphysical characteristics of three anvils sampled during the Central Equatorial Pacific Experiment (CEPEX). *J. Atmos. Sci.* **53**: 2401–2423.

McFarquhar GM, Zhang G, Poellot MR, Kok GL, McCoy R, Tooman T, Fridlind A, Heymsfield AJ. 2007. Ice properties of single-layer stratocumulus during the Mixed-Phase Arctic Cloud Experiment: 1. Observations. *J. Geophys. Res.* **112**: D24201, doi:10.1029/2007JD008633.

McFarquhar G, Baumgardner D, Bansemer A, Abel S, Crosier J, French J, Rosenberg P, Korolev A, Schwarzenboeck A, Leroy D, Um J, Wu W, Heymsfield A, Twohy C, Detwiler A, Field P, Neumann A, Axisa D, Cotton R, Dong J. 2017. Processing of Cloud In-Situ Data Collected by Bulk Water, Scattering, and Imaging Probes: Fundamentals, Uncertainties and Efforts towards Consistency. *Meteor. Monogr*. Under revision.

Mitchell D, Heymsfield A. 2005. Refinements in the treatment of ice particle terminal velocities, highlighting aggregates. *J. Atmos. Sci.*, **62**: 1637–1644, doi:10.1175/JAS3413.1.

Morrison AE, Siems ST, Manton MJ, Nazarov A. 2010. A modeling case study of mixed-phase clouds over the Southern Ocean and Tasmania. *Mon. Wea. Rev.* **138**(3): 839-862, doi: 10.1175/2009MWR3011.1.

Mossop SC, Ono A, Wishart ER. 1970. Ice particles in maritime clouds near Tasmania. *Q. J. R. Meteorol. Soc.* **96**: 487-508.

Mossop SC, Hallett J. 1974. Ice crystal concentration in cumulus clouds: Influence of the drop spectrum. *Science*. **186**: 632-634.

Mossop SC. 1985. Secondary ice particle production during rime growth: The effect of droplet size distribution and rimer velocity. *Q. J. R. Meteorol. Soc.* **11**: 1113-1124.

Muhlbauer A, McCoy IL, Wood R. 2014. Climatology of stratocumulus cloud morphologies: microphysical properties and radiative effects. *Atmos. Chem. Phys.* **14**: 6695–6716.

O'Dowd C, Smith M, Consterdine I, Lowe J. 1997. Marine aerosol, sea-salt, and the marine sulphur cycle: A short review. *Atmos. Environ.* **31**: 73-80.

Omar AH, and coauthors. 2009. The CALIPSO automated aerosol classification and lidar ratio selection algorithm. *J. Atmos. Oceanic Technol.* **26**: 1994-2014, doi:10.1175/2009JTECHA1231.1.

Oraltay RG, Hallett J. 2005. The melting layer: a laboratory investigation of ice particle melt and evaporation near 0ºC. *J. Appl. Meteorol.* **44**: 206-220.

Ovtchinnikov M, Kogan YL, Blyth AM. 2000. An investigation of ice production mechanisms in small cumuliform clouds using a 3D cloud model with explicit microphysics. Part II: Case study of New Mexico cumulus clouds. *J. Atmos. Sci.* **57**: 3004-3021.

Partain P. 2007. Cloudsat ECMWF-AUX auxiliary data process description and interface control document. Cooperative Institute for Research in the Atmosphere, Colorado State University, 11 pp.

Platnick S, King MD, Ackerman SA, Menzel WP, Baum BA, Riédi JC, Frey RA. 2003. The MODIS cloud products: Algorithms and examples from Terra. IEEE Trans. *Geosci. Remote Sens.* **41**: 459-473, doi: 10.1109/TGRS.2002.808301.

Prenni AJ,   Coauthors. 2007. Can ice-nucleating aerosols affect Arctic seasonal climate? *Bull. Am. Meteorol. Soc.* **88**: 541–550, doi:10.1175/BAMS-88-4-541.

Pruppacher, HR, Klett JD. 1997. Microphysics of Clouds and Precipitation, 2nd ed., *Kluwer Acad., Norwell, Mass.* 954.

Ryan, BF, Wishart ER, Shaw DE. 1976. The growth rates and densities of ice crystals between -3 and -21ºC. *J. Atmos. Sci.*, **33**: 842-850.

Saunders C, Hosseini A. 2001. A laboratory study of the effect of velocity on Hallett – Mossop ice crystal multiplication. *Atmos. Res.* **59**: 3-14.

Shupe MD, Uttal T, Matrosov S, Frisch AS. 2001. Cloud water contents and hydrometeor sizes during the FIRE Arctic Clouds Experiment. *J. Geophys. Res.* **106**: 15015-15028.

Siems ST, Hess GD, Suhre K, Businger S, Draxler RR. 2000. The impact of wind shear on observed and simulated trajectories during the ACE-1 Lagrangian experiments. *Aust. Met. Mag.* **49**: 109-120.

Stephens GL, Vane DG, Boain RJ, Mace GG, Sassen K, Wang Z, Illingworth AJ, O'Connor EJ, Rossow WB, Durden SL, Miller SD, Austin RT, Benedetti A, Mitrescu C, CloudSat Science Team. 2002. The CloudSat mission and the A-Train: A new dimension of space-based observations of clouds and precipitation. *Bull. Am. Meteorol. Soc.* **83**: 1771–1790, doi: 10.1175/BAMS-83-12-1771.

Stephens GL, and coauthors. 2010. Dreary state of precipitation in global models. *J. Geophys. Res.* **115**: D24211, doi:10.1029/2010JD014532.

Stevens B, Vali G, Comstock K, Wood R, VanZanten M, Austin P, Bretherton C, Lenschow D. 2005. Pockets of Open Cells (POCs) and drizzle in marine stratocumulus. *Bull. Am. Meteorol. Soc*. **86**: 51-57.

Strapp JW, Oldenburg J, Ide R, Lilie L, Bacic S, Vukovic Z, Oleskiw M, Miller D, Emergy E, Leone G. 2003. Wind tunnel measurements of the response of hot-wire liquid water content instruments to large droplets. *J. Atmos. Oceanic Technol.* **20**: 791–806.

Takahashi T, Nagano Y, Kushiyama Y. 1995. Possible high ice particle production during graupel-graupel collisions. *J. Atmos. Sci.* **52**: 4523- 4527.

Tanelli S, Durden SL, Im E, Pak KS, Reinke D, Partain P, Marchand R, Haynes J. 2008. CloudSat's cloud profiling radar after 2 years in orbit: Performance, external calibration, and processing. *IEEE Trans. Geosci. Remote Sens.* **46**: 3560-3573.

Taylor JW, Choularton TW, Blyth AM, Liu Z, Bower KN, Crosier J, Gallagher MW, Williams PI, Dorsey JR, Flynn MJ, Bennett LJ, Huang Y, French J, Korolev A, Brown PRA. 2016. Observations of cloud microphysics and ice formation during COPE. *Atmos. Chem. Phys*. **16**: 799-826, doi:10.5194/acp-16-799-2016, 2016.

Trenberth KE, Fasullo JT. 2010. Simulation of present-day and twenty-first-century energy budgets of the Southern Oceans. *J. Clim.* **23**: 440–454, doi:10.1175/2009JCLI3152.1.

Vinoth J, Young IR. 2011. Global estimates of extreme wind speed and wave height. *J. Clim.* **24**(6): 1647–1665, doi:10.1175/2010JCLI3680.1.

Wang H, Feingold G. 2009. Modeling mesoscale cellular structures and drizzle in marine stratocumulus. Part I: Impact of drizzle on the formation and evolution of open cells. *J. Atmos. Sci.*, **66**: 3237–3256.

Wang Z, Siems ST, Belusic D, Manton MJ, Huang Y. 2015. A Climatology of the Precipitation over the Southern Ocean as Observed at Macquarie Island. J. Appl. Meteor. **54**(12): 2321-2337.

Weller R, Schmidt K, Teinilä K, Hillamo R. 2015. Natural new particle formation at the coastal Antarctic site Neumayer. *Atmos. Chem. Phys.* **15**: 11399-11410, doi:10.5194/acp-15-11399-2015.

Wendisch M, Brenguier J-L (Eds.). 2013: Airborne Measurements for Environmental Research: Methods and Instruments. *Wiley-VCH Verlag GmbH & Co. KGaA*, Weinheim, Germany. ISBN: 978-3-527-40996-9. 655 pp, doi: 10.1002/9783527653218

Wilson TW, and coauthors. 2015. A marine biogenic source of atmospheric ice-nucleating particles. *Nature*. **525** (7568): 234-238.

Winker DM, Hunt BH, McGill MJ. 2007. Initial performance assessment of CALIOP. *Geophys. Res. Lett.* **34**: L19803, doi: 10.1029/2007GL030135.

Wolters ELA, Deneke HM, van den Hurk BJJM, Meirink JF, Roebeling RA. 2010. Broken and inhomogeneous cloud impact on satellite cloud particle effective radius and cloud-phase retrievals. *J. Geophys. Res.* **115**: D10, doi: 10.1029/2009JD012205.

Wood R. 2012. Stratocumulus Clouds. *Mon. Weather Rev.* **140**: 2373-2423.

Wood R, Leon D, Lebsock M, Snider J, Clarke AD. 2012. Precipitation driving of droplet concentration variability in marine low clouds. *J. Geophys. Res.* **117**: D19210, doi:10.1029/2012JD018305.

Wood R, Hartmann DL. 2006. Spatial variability of liquid water path in marine low cloud: The importance of mesoscale cellular convection. *J. Clim.* **19**: 1748-1764.

Zeng S, Cornet C, Parol F, Reidi J, Thieuleux F. 2012. A better understanding of cloud optical thickness derived from the passive sensors MODIS/AQUA and POLDER/PARASOL in the A-Train constellation. *Atmos. Chem. Phys.* **12**: 11245-11259, doi:10.5194/acp-12-11245-2012.

Zuidema P, Baker B, Han Y, Intrieri J, Key J, Lawson P, Matrosov S, Shupe M, Stone R, Uttal T. 2005. An Arctic springtime mixed-phase cloudy boundary layer observed during SHEBA. *J. Atmos. Sci.* **62**: 160-176.

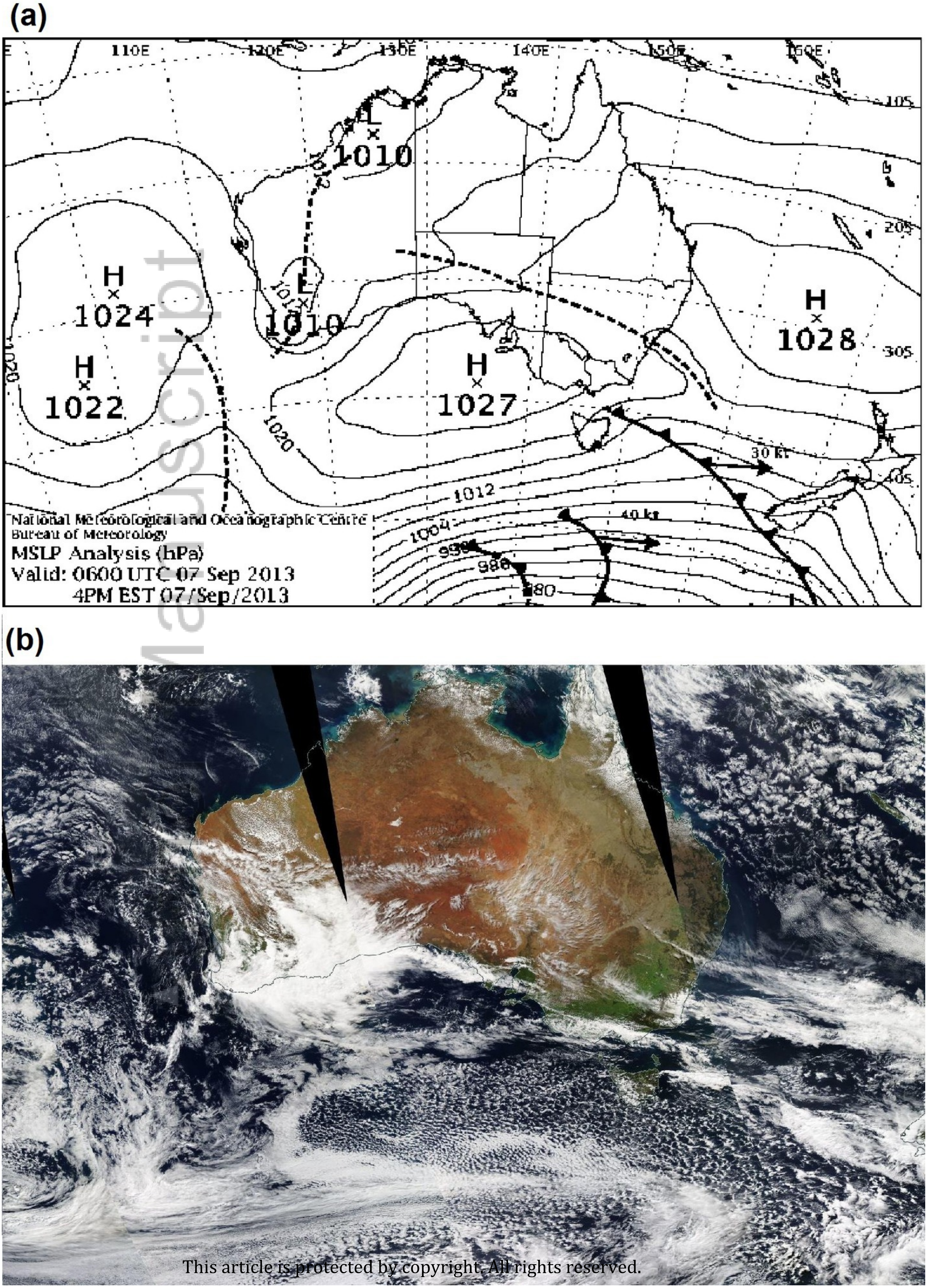
(a)
110E
120E
130E
140E
150E
160E
10S
20S
30S
40S
L
1010
1012
H
1024
H
1022
L
1010
1012
1020
H
1027
H
1028
1020
1012
1004
996
988
980
30 kt
40 kt
National Meteorological and Oceanographic Centre
Bureau of Meteorology
MSLP Analysis (hPa)
Valid: 0600 UTC 07 Sep 2013
4PM EST 07/Sep/2013
(b)

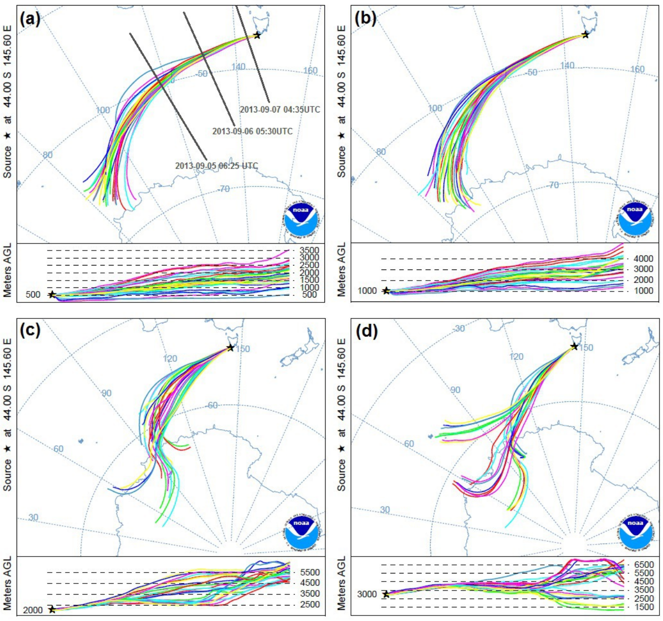

Figure 2. Back_trajectories.jpg

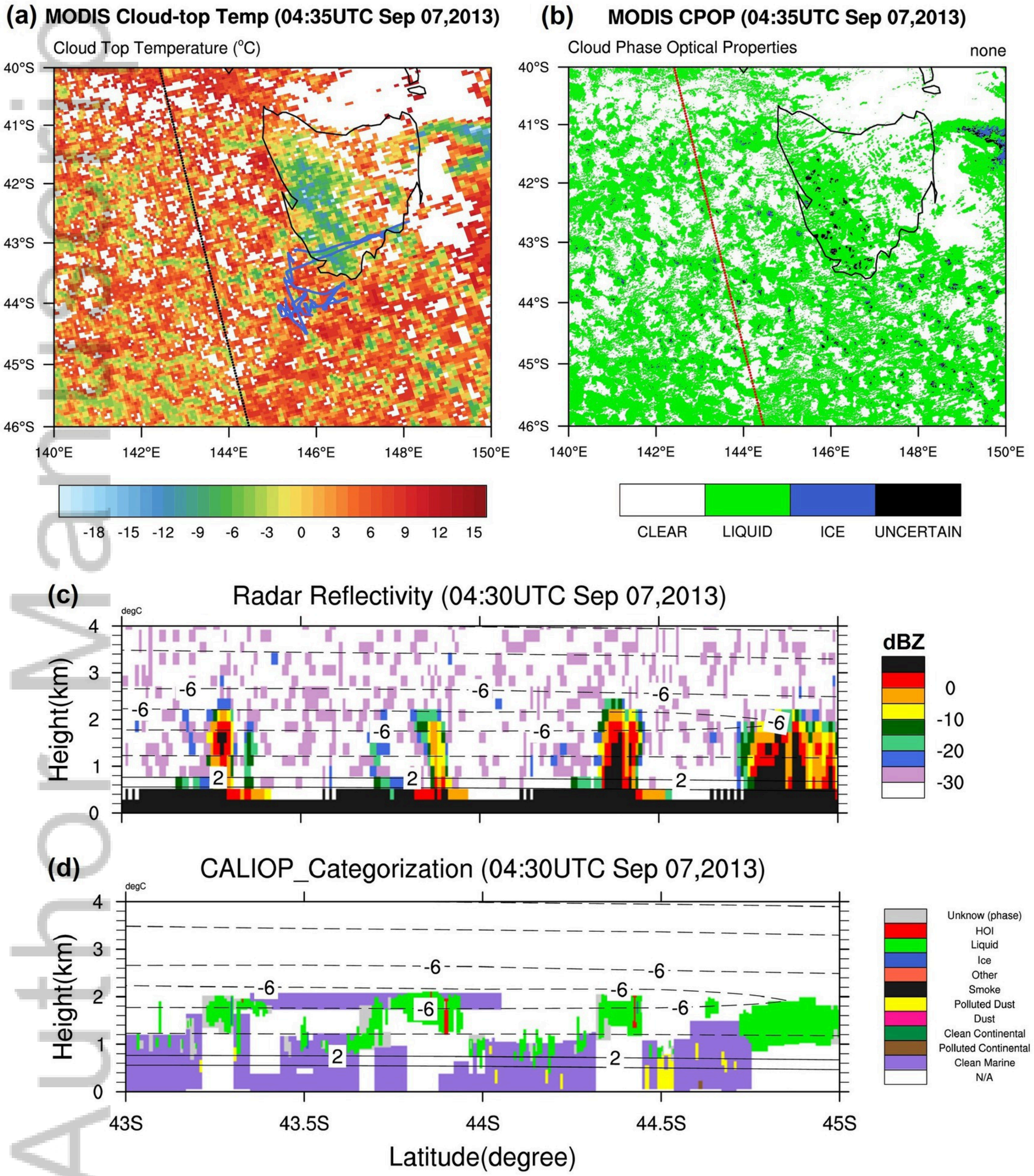

Figure 3. A-Train_20130907.jpg

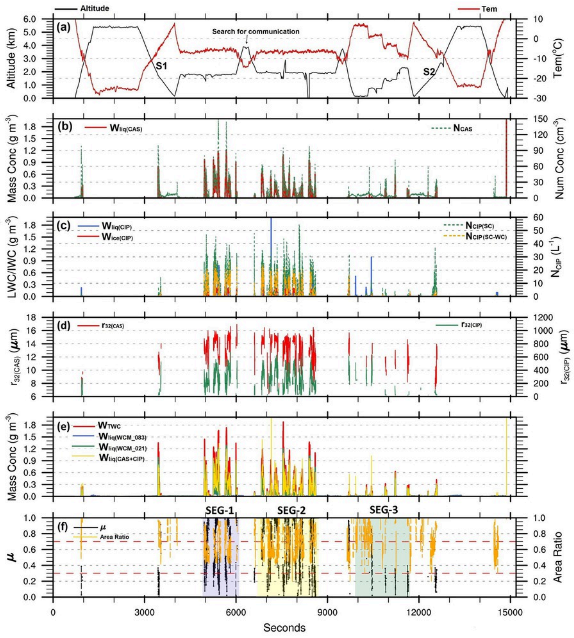

Figure 4. Time_series_whole_flight.jpg

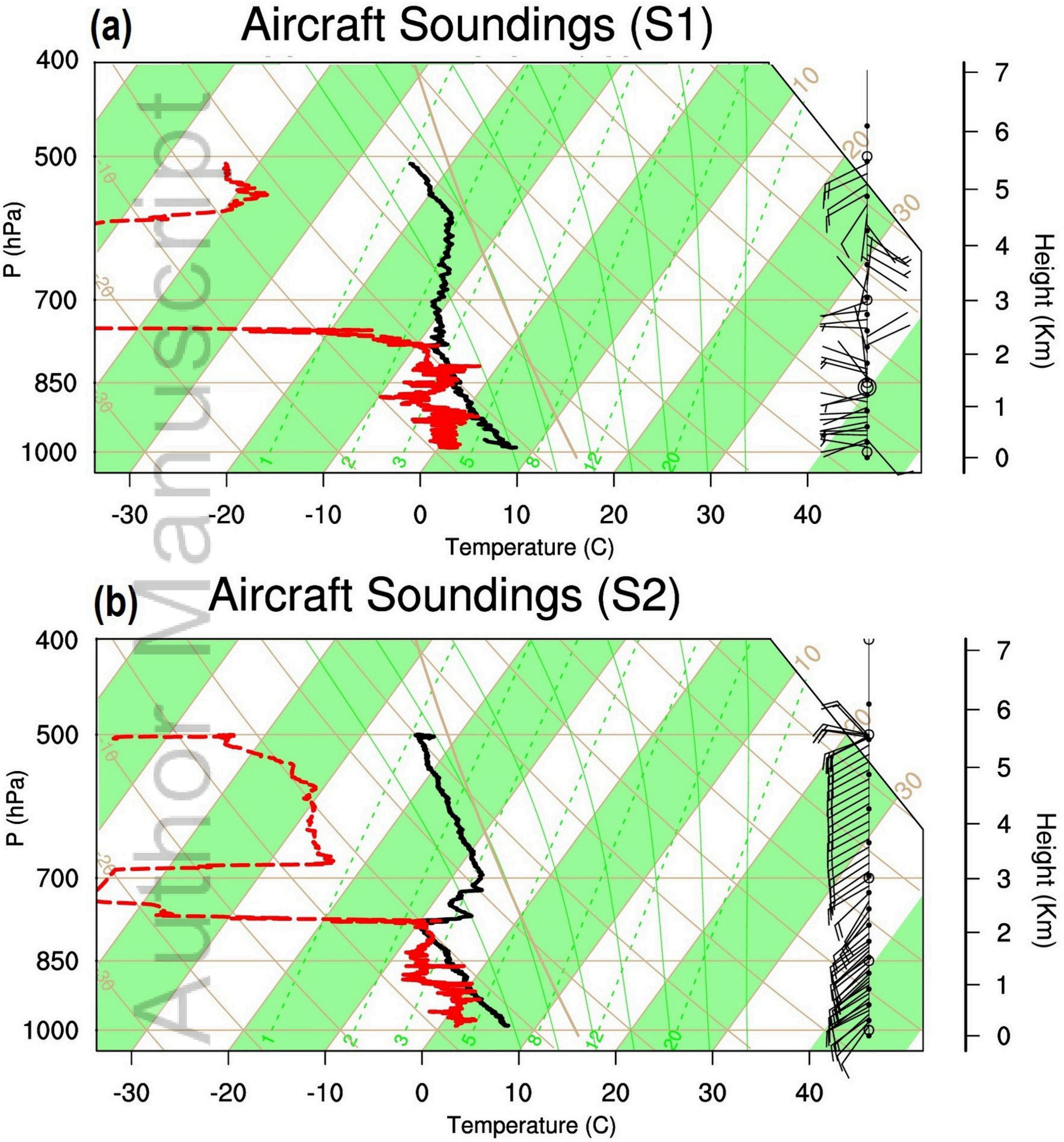

Figure 5. Sounding_merged.jpg

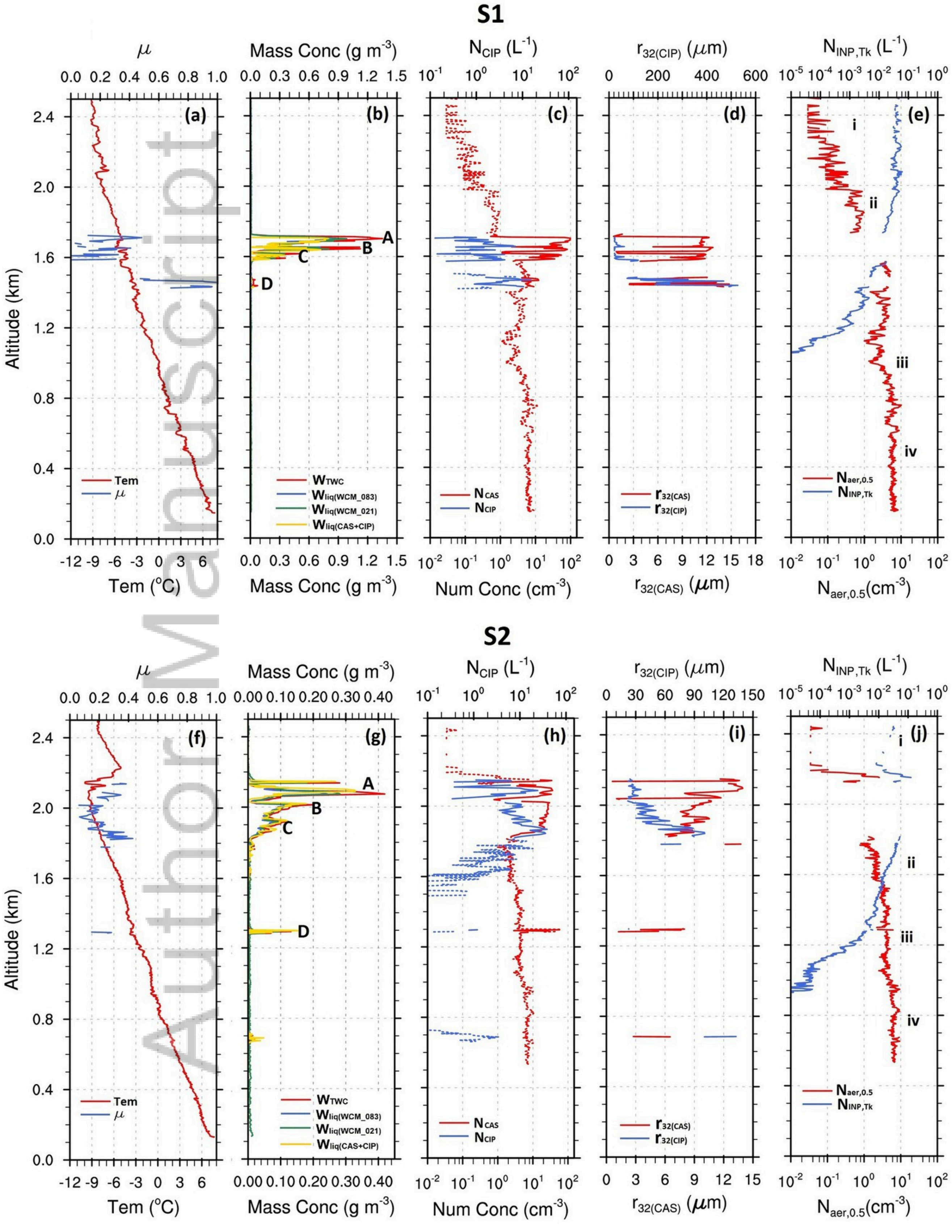

Figure 6. All_profiles_merged.jpg

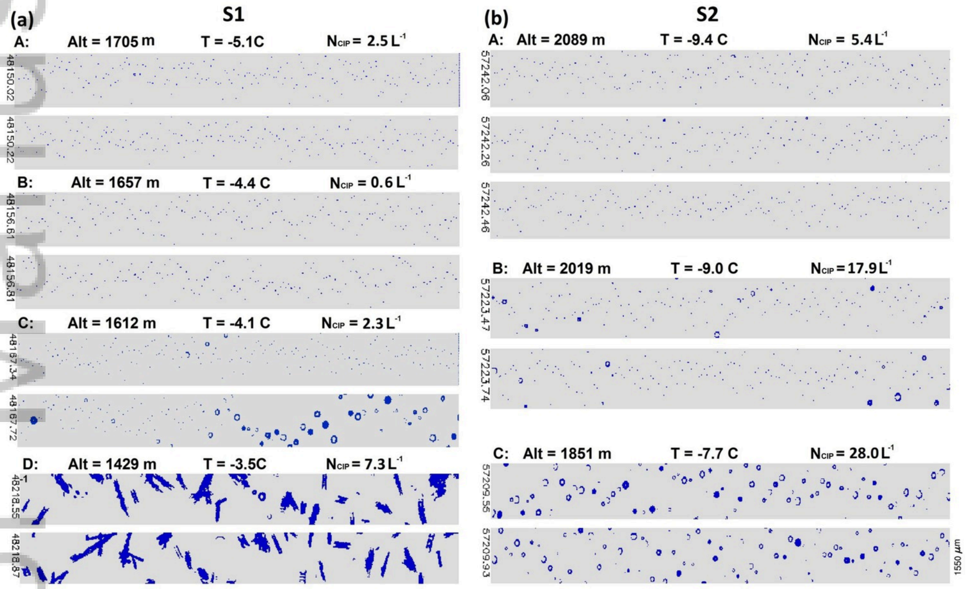

Figure 7. CIP_images_sounding_merged.jpg

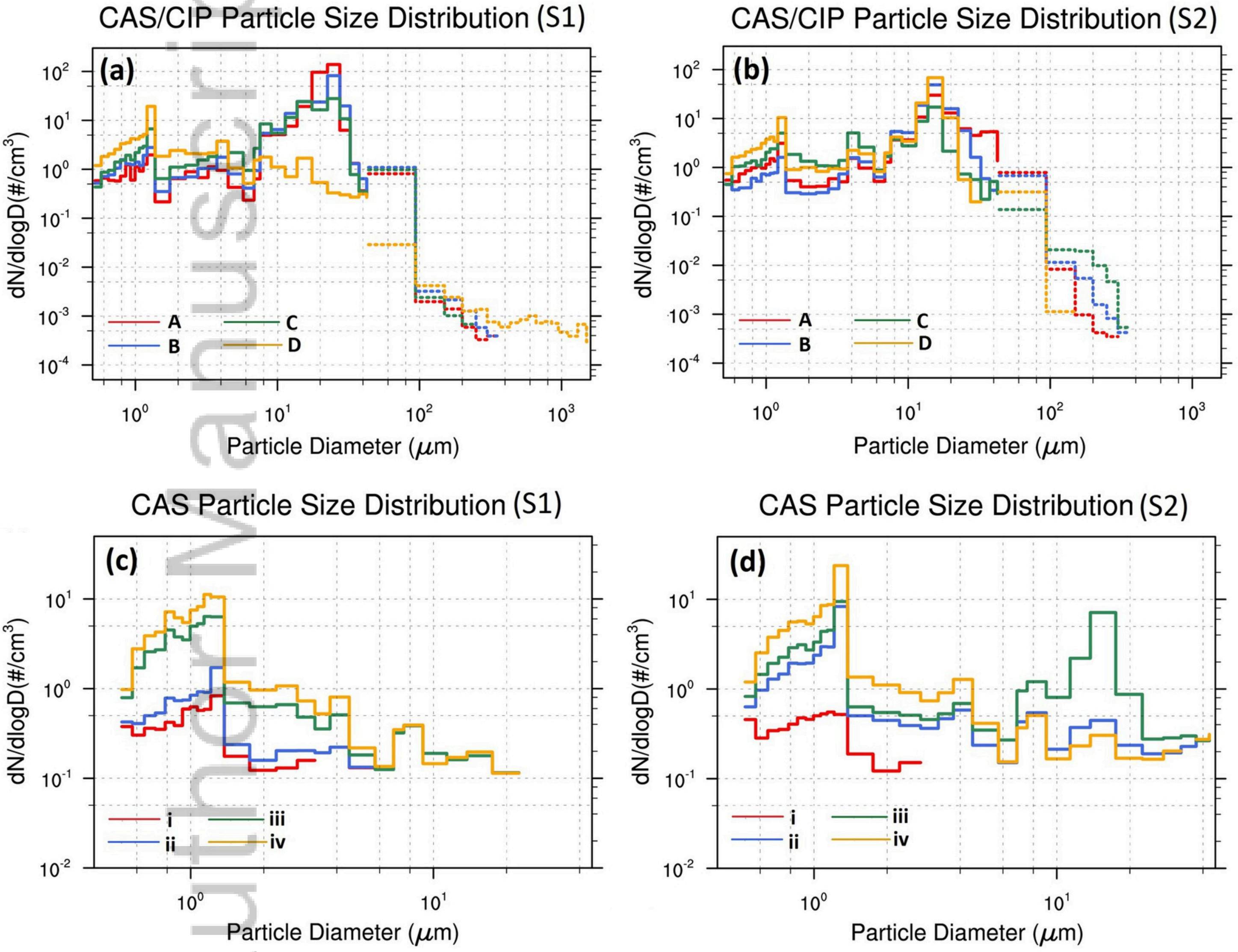

Figure 8. Spectrums_merged.jpg

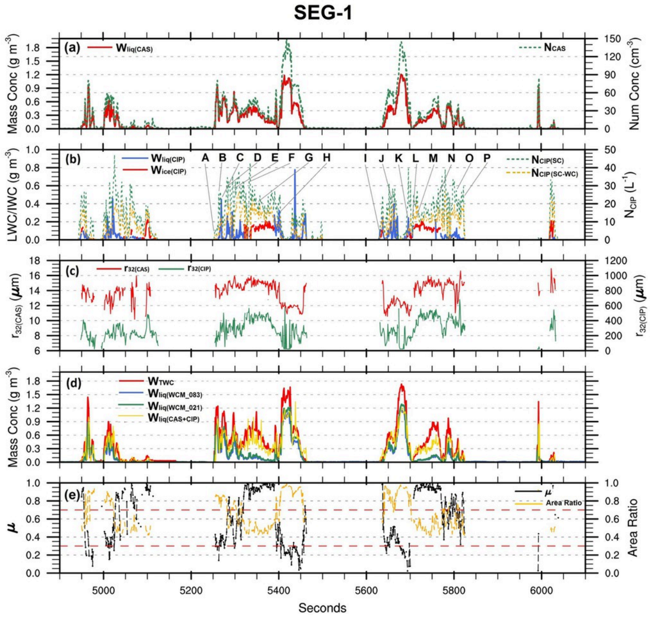

Figure 9. Time_series_SEG-1.jpg

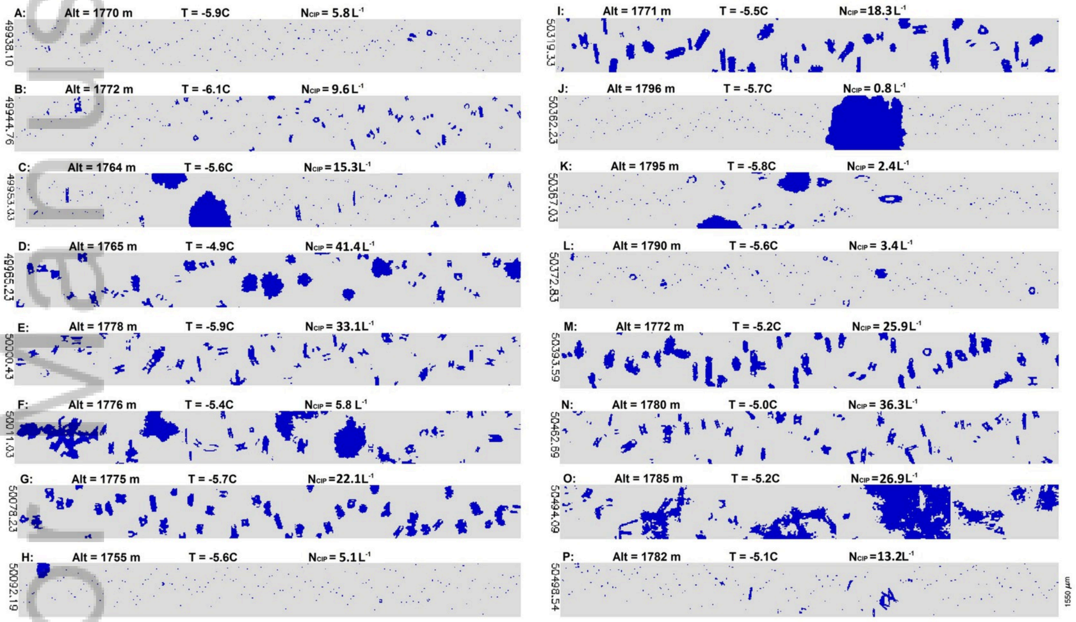

Figure 10. CIP_images_SEG-1.jpg

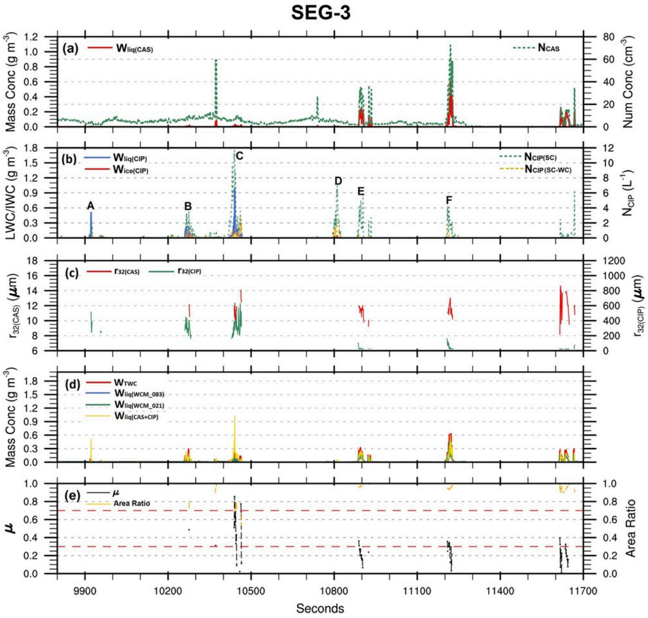

Figure 11. Time_series_SEG-3.jpg

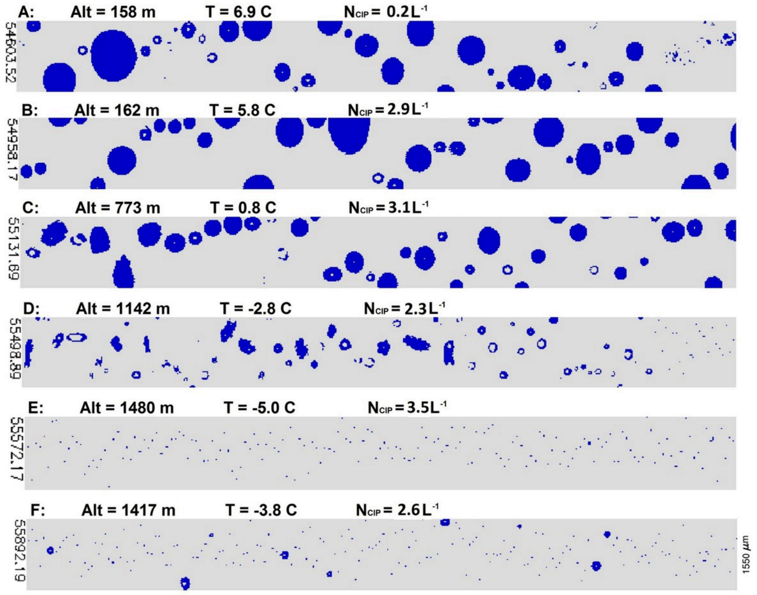

Figure 12. CIP_images_SEG-3.jpg

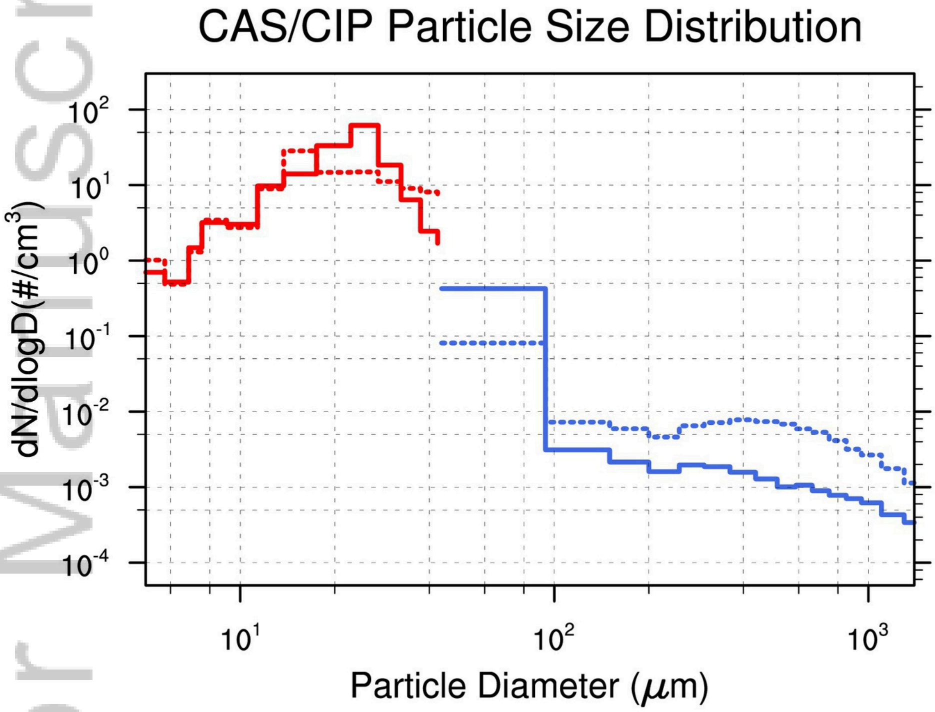

Figure 13. CAS_CIP_spectrum_all_bins_liquid_mixed.jpg

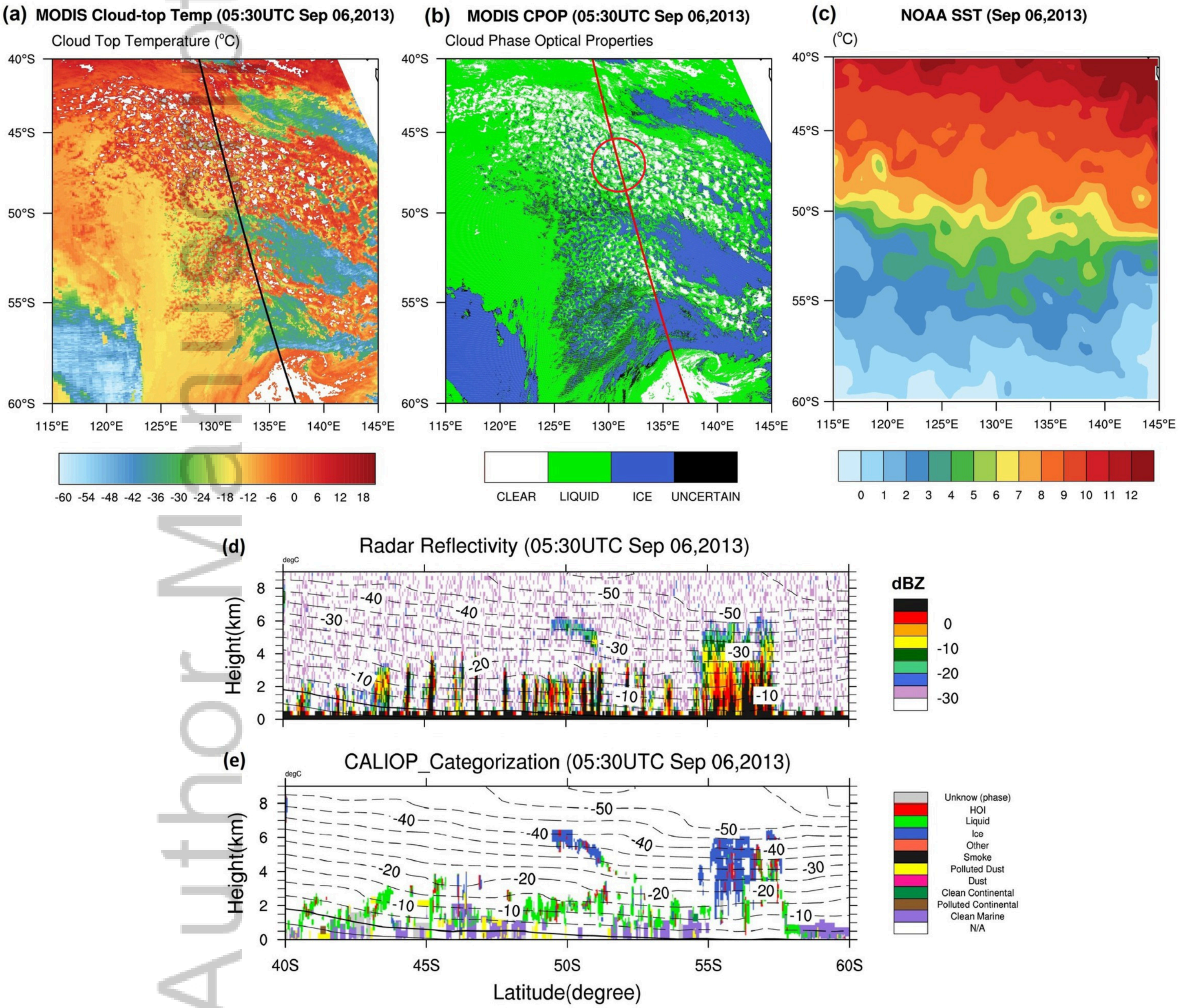

Figure 14. A-Train_20130906.jpg

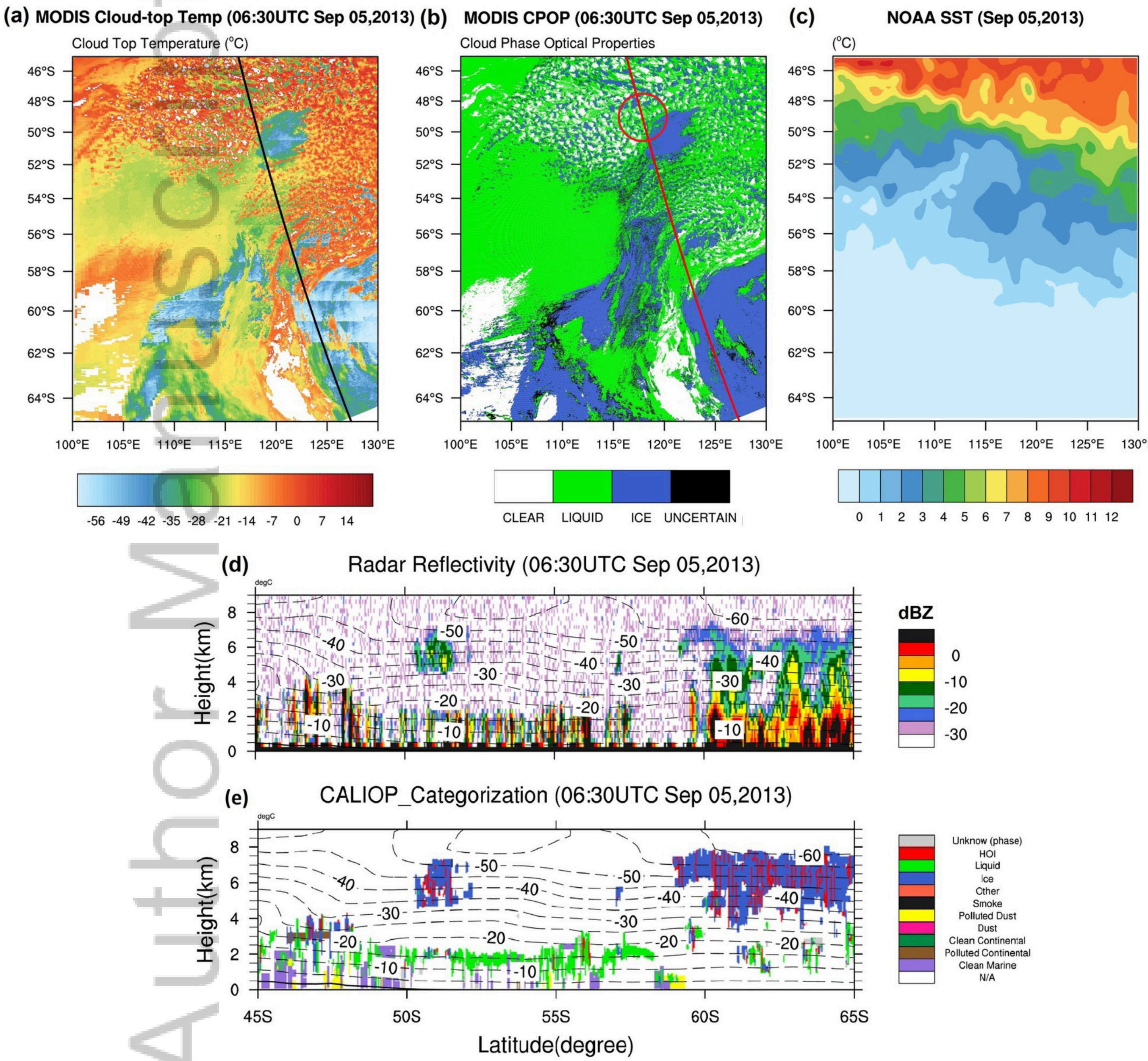

Figure 15. A-Train_20130905.jpg